Open Research Online

Effective elastic properties of 3D stochastic bicontinuous composites

Journal Item

oro.open.ac.uk

Research paper

Effective elastic properties of 3D stochastic bicontinuous composites

Celal Soyarslan[*,a], Marc Pradas[b], Swantje Bargmann[a]

[a] *Chair of Solid Mechanics, School of Mechanical Engineering and Safety Engineering, University of Wuppertal, Germany*
[b] *School of Mathematics and Statistics, The Open University, Milton Keynes MK7 6AA, United Kingdom*

A B S T R A C T

We study effective elastic properties of 3D bicontinuous random composites (such as, e.g., nanoporous gold filled with polymer) considering linear and infinitesimal elasticity and using asymptotic homogenization along with the finite element method. For the generation of the microstructures, a leveled-wave model based on the works of Cahn (1965) and Soyarslan et al. (2018) is used. The influences of volume element size, phase contrast, relative volume fraction of phases and applied boundary conditions on computed apparent elastic moduli are investigated. The nanocomposite behaves distinctly different from its nanoporous counterpart as determined by scrutinized macroscopic responses of gold-epoxy nanocomposites of various phase volume fractions. This is due to the fact that, in space-filling nanocomposites the force transmission is possible in all directions whereas in the nanoporous gold the load is transmitted along ligaments, which hinges upon the phase topology through network connectivity. As a consequence, we observe a distinct elastic scaling law for bicontinuous metal-polymer composites. A comparison of our findings with the Hashin-Shtrikman, the three-point Beran-Molyneux and the Milton-Phan-Tien analytical bounds show that computational homogenization using periodic boundary conditions is justified to be the only tool in accurate and efficient determination of the effective properties of 3D bicontinuous random composites with high contrast and volume fraction bias towards the weaker phase.

1. Introduction

Heterogeneous materials composed of domains of different phases with highly contrasting mechanical properties abound in synthetic products and nature. Nanoporous bicontinuous metal-polymer composites manufactured based on dealloying are heterogeneous materials with low metallic phase volume content (usually < 0.30). The main load carrying metallic phase reveals an open-cell morphology formed of interconnected ligaments. Due to strong size effects emerging at this scale length (e.g., excess surface elasticity and surface tension), these ligaments behave as ultra high-strength nanowires (Biener et al., 2006; Elsner et al., 2017). Their unique properties such as high yield strength despite high porosity, large specific surface area and electrocatalytic performance make these highly functional materials popular in applications of optical-active materials, catalysts, sensors, mechanical actuators, fuel cells and microbalance electrodes, and as a coating for medical devices (Weissmüller et al., 2003; Erlebacher et al., 2001; Chen et al., 2010). Even though considerable work has been done

towards understanding the kinetics of phase separation during dealloying, a full comprehension of the mechanical properties of nanoporous metals and their composites still eludes us (Biener et al., 2005; 2006; Rösner et al., 2007; Hodge et al., 2007; Zinchenko et al., 2013; Saane et al., 2014; Carolan et al., 2015; McCue et al., 2016; Lührs et al., 2016; Soyarslan et al., 2018b; Jiao and Huber, 2017; Griffiths et al., 2017; Soyarslan et al., 2018a; Yang et al., 2018; Leitner et al., 2018; Griffiths et al., 2017; Bargmann et al., 2016; Wang et al., 2011; Wang and Weissmüller, 2013; Wang, 2015; Weissmüller et al., 2009; Volkert et al., 2006; Mameka et al., 2016; Hu et al., 2016; Hu, 2017; Huber et al., 2014). Computer simulation proves to be powerful for this aim (Xia et al., 2015), but still one grand difficulty in this context is making the highly complicated microstructure of the material accessible (Bargmann et al., 2018; Soyarslan et al. 2018b).

In this work, we study the effective elastic properties of 3D bicontinuous random composites considering linear and infinitesimal elasticity making use of asymptotic homogenization along with a finite element method.[1] For the generation of the 3D bicontinuous random

---

* Corresponding author.
    E-mail address: soyarslan@uni-wuppertal.de (C. Soyarslan).
[1] The use of asymptotic analysis in the context of our study allows obtaining effective elastic properties and resolving stresses at constituent materials at microscale in bicontinuous composites considering linear elastostatics and two scales. Its application, however, can be extended to non-linear analysis, covering both geometric and material nonlinearities, as well as to several scales and for various physical phenomena. For a detailed discussion, (see Fish and Fan, 2008; Fish et al., 1997; Markenscoff and Dascalu, 2012; Yang et al., 2013; Fish, 2014) and the references therein.

microstructures, a leveled-wave model is devised. Leveled-wave models for random morphologies, as was conceived by Cahn (1965) as a modeling tool for material systems involving phase separation (and hence bicontinuous morphologies) have the following advantages: (i) it warrants an efficient, yet sufficiently representative, generation of spinodal-like microstructures in short times (Soyarslan et al., 2018b), especially as compared to phase field methodologies that model spinodal decomposition (Sun et al., 2013); and (ii) it allows analytical computation of certain topological and morphological properties for the generated microstructures, e.g., average Gaussian curvature and mean curvature, surface-to-bulk volume ratio and genus (Teubner, 1991; Berk, 1991; Soyarslan et al., 2018b). Especially the Gaussian random field property of the truncated Fourier series allows an a priori determination of the level of a desired solid volume fraction which is one of the most important morphological descriptors of heterogeneous materials (Torquato, 2002).

We investigate the influence of the volume element size, phase contrast, relative volume fraction of phases and applied boundary conditions on apparent elastic moduli and anisotropy index. As anticipated, with increasing volume element size, the apparent properties converge to effective ones and the bicontinuos composite tends to exhibit elastic isotropy. Our results conform excellently with the elastic scaling law proposed for spinodal decomposition-based bicontinuous microstructures (Carolan et al., 2015). Only under periodic boundary conditions, effective properties can be determined at a reasonably small volume element size, hereby referred to as the representative volume element (RVE) size. At this size, the overestimating property of kinematic uniform boundary conditions is shown where the prediction gap is observed to increase with increasing phase contrast and volume fraction bias towards the weaker phase. Nevertheless, the estimations by analytical bounds of Hashin-Shtrikman, three-point Beran-Molyneux and Milton-Phan-Tien on elastic moduli are observed to be much less accurate as compared to the results of both boundary conditions. Thus, computational homogenization using periodic boundary conditions is observed to be a seamlessly accurate and efficient tool in determination of the effective properties of 3D bicontinuous random composites with high contrast and volume fraction bias towards the weaker phase and even for nonperiodic structures lacking translational symmetry by homogenization convergence since the random media at hand is statistically homogeneous and ergodic (Sab and Nedjar, 2005; Terada et al., 2000).

2. Elastostatics of bicontinuous random composites

2.1. Continuum with microstructure and its numerical generation

We start by introducing the notions of a continuum with microstructure and the computational micro-to-macro transition (Miehe and Koch, 2002; McBride et al., 2012) as shown in Fig. 1. Let $\mathcal{B} \subset \mathcal{R}^3$ denote the homogenized macrocontinuum, a typical point ${}^{M}\boldsymbol{x} \in \mathcal{B}$ of which

encapsulates a microstructure, represented by the unit cell domain $\mathcal{V} \subset \mathcal{R}^3$ consisting of two constituent material domains $\mathcal{V}_1 \subset \mathcal{V}$ and $\mathcal{V}_2 \subset \mathcal{V}$. More precisely, the coordinate ${}^{M}\boldsymbol{x}$ represents the macroscale position vector which is also referred to as the global or slow variable. Then, we denote the microscale position vector which is also referred to as the local or fast variable by $\boldsymbol{x}$. Both variables are related through $\boldsymbol{x} = {}^{M}\boldsymbol{x}/\epsilon$ where $0 < \epsilon \ll 1$ controls the fineness (scale separation) of the volume element structure. Thus, if ϵ is small, then the microstructure is fine and the property functions show rapid oscillations. We consider random microstructural morphologies formed through spinodal decomposition - a process where a solution of $n \geq 2$ components rapidly decomposes into distinct coexisting phases. In the Cahn–Hilliard formulation (Cahn and Hilliard, 1959), the Helmholtz free energy of a small volume of a two-component inhomogeneous solution is given by $\Psi = \int_{\mathcal{V}} [g(c) + [\kappa^2/2] |\nabla_{\boldsymbol{x}} c|^2] dV$, where $g(c)$ denotes the free energy density of a homogeneous material of composition c, and the square gradient term represents the additional free energy density due to the inhomogeneous composition. Hence, this ensures the existence of a well-defined interface between both phases whose spatial extension is governed by the parameter κ. Here, $\nabla_{\boldsymbol{x}}$ and $\mathrm{div}_{\boldsymbol{x}}$ respectively denote the gradient and the divergence with respect to the microscopic coordinate $\boldsymbol{x}$. The dynamics of the concentration is then given by a generalized diffusion equation

$$\frac{\partial c}{\partial t} = \mathrm{div}_{\boldsymbol{x}}(M \nabla_{\boldsymbol{x}} \mu_{\mathrm{c}}) = M \mathrm{div}_{\boldsymbol{x}} \nabla_{\boldsymbol{x}} [g'(c) - \kappa^2 \mathrm{div}_{\boldsymbol{x}} \nabla_{\boldsymbol{x}} c], \tag{1}$$

where $M > 0$ denotes the mobility and $\mu_{\mathrm{c}} = \delta\Psi/\delta c$ is the chemical potential. The solution of the above equation in the early stages of spinodal decomposition can be described in terms of a superposition of standing sinusoidal waves of fixed wavelength but random in amplitude, direction and phase (Cahn, 1965), see also Soyarslan et al. (2018b), represented by a truncated Fourier series:

$$f(\boldsymbol{x}) = \frac{1}{\sqrt{N}} \sum_{i=1}^{N} a_i \cos(\boldsymbol{q}_i \cdot \boldsymbol{x} + \varphi_i). \tag{2}$$

Here, $f(\boldsymbol{x}) = [c(\boldsymbol{x}) - c_0]/c_s$ with $\boldsymbol{x}$ denoting the position vector, c_0 is the average composition and c_s is the scaling parameter.

N represents the number of waves considered in the truncated series. Moreover, a_i, $\boldsymbol{q}_i$ and φ_i denote the wave amplitude, wave direction and wave phase of the ith wave, respectively. We consider a constant value for the amplitude, namely $a_i = \sqrt{2}$, and a fixed wave number with $q_i = |\boldsymbol{q}_i| = q_0$. The wave phases are uniformly distributed on $[0, 2\pi)$ and the wave directions are uniformly distributed over the solid angle 4π.

Under these conditions $f(\boldsymbol{x})$ is a Gaussian random function with $\langle f \rangle = 0$, $\langle f^2 \rangle = 1$, where brackets denote ensemble averages over realizations. For N sufficiently large, the value of the random function $f(\boldsymbol{x})$ follows a Gaussian distribution with $P(f) = e^{-f^2/2}/\sqrt{2\pi}$. Given the random function (2) the different phases of the system are then defined via a selected level cut ξ:
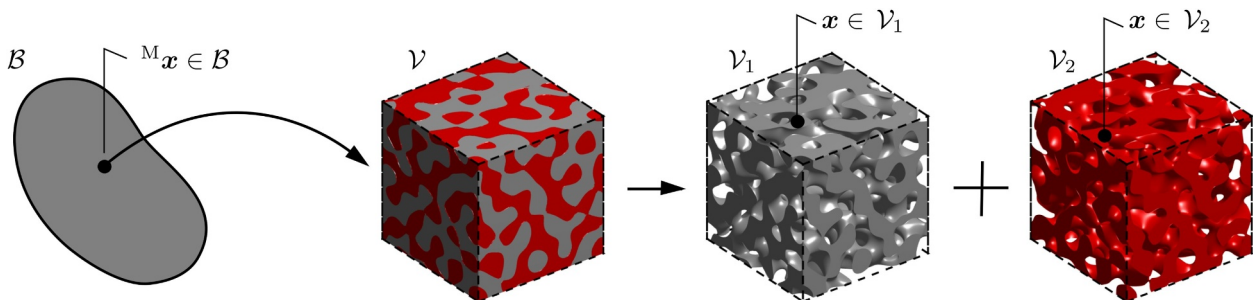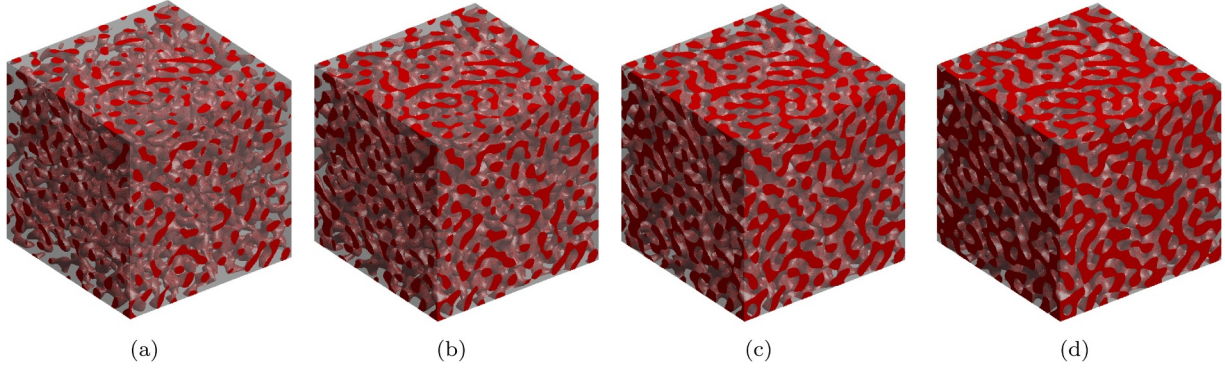

Fig. 1. Considered continuum with microstructure. $\mathcal{B} \subset \mathcal{R}^3$ denotes the domain of the homogenized macrocontinuum. A typical point ${}^{M}\boldsymbol{x} \in \mathcal{B}$ encapsulates a unit cell (representative volume) domain $\mathcal{V} \subset \mathcal{R}^3$, composed of two constituent domains $\mathcal{V}_1 \subset \mathcal{V}$ and $\mathcal{V}_2 \subset \mathcal{V}$ of different materials, at the microscale. Domain coordinates ${}^{M}\boldsymbol{x}$ and $\boldsymbol{x}$ are related through $\boldsymbol{x} = {}^{M}\boldsymbol{x}/\epsilon$ where $0 < \epsilon \ll 1$ controls the fineness of the volume element structure. The superscript M stands for macroscale.

Fig. 2. Examples of bicontinuous microstructures generated with the level cut method Soyarslan et al. (2018b) for phase 1 (red) / phase 2 (grey - transparent) volume fractions of (a) $\phi_1 = 0.20$, (b) $\phi_1 = 0.30$, (c) $\phi_1 = 0.40$, (d) $\phi_1 = 0.50$; volume element size of 12 wavelengths. (For interpretation of the references to colour in this figure legend, the reader is referred to the web version of this article.)

$$\begin{aligned} \boldsymbol{x} \in \mathcal{V}_1 \quad &\text{if} \quad f(\boldsymbol{x}) < \xi, \\ \boldsymbol{x} \in \iota \quad &\text{if} \quad f(\boldsymbol{x}) = \xi, \\ \boldsymbol{x} \in \mathcal{V}_2 \quad &\text{if} \quad f(\boldsymbol{x}) > \xi, \end{aligned} \tag{3}$$

where ι denotes the interface of phases $\mathcal{V}_1$ and $\mathcal{V}_2$. A priori determination of ξ for a desired phase volume fraction for phase 1, denoted by ϕ_1, can be realized exploiting the Gaussian property of the random field and using

$$\xi(\phi_1) = \sqrt{2} \, \text{inverf}(2\phi_1 - 1), \tag{4}$$

where inverf(x) represents the inverse error function. Examples of generated microstructures for different values of ξ are depicted in Fig. 2.

As discussed in detail in Bargmann et al. (2018), besides being random, bicontinuous composite microstructures can also be ordered. Triply periodically architected polymer composites with interpenetrating phases constitute examples of ordered structures obtained through manufacturing (Al-Ketan et al., 2017). In nature, e.g., skeletons of sea urchin (Lai et al., 2007), butterfly wings (Michielsen and Stavenga, 2008) and certain self-assembled block copolymers (Bates et al., 1994) have ordered bicontinuous structures in which the phase interface geometrical features resemble triply periodic minimal surfaces (Lai et al., 2007). Bicontinuous microstructures studied in this work are generally neither ordered nor periodic. It is possible to attain periodicity while keeping the stochastic nature of the phase distribution (Soyarslan et al., 2018b). One way to obtain f with translational periodicity with lattice vectors of magnitude a with $f(\boldsymbol{r}) = f(\boldsymbol{r} + ma\boldsymbol{e}_1 + na\boldsymbol{e}_2 + oa\boldsymbol{e}_3)$ for arbitrary integers m, n, o is to select a finite number of waves $\boldsymbol{q}_i$ with integer wave number in all directions and constant modulus. To this end, letting the integers h, k, l denote Miller indices, a a constant and $\boldsymbol{e}_1, \boldsymbol{e}_2, \boldsymbol{e}_3$ unit vectors of an orthonormal basis in real space, $\boldsymbol{q}_i$ should have the form $\boldsymbol{q} = [2\pi/a](h, k, l)$.

2.2. Homogenization theory

The asymptotic homogenization method used here is similar to that described in Lukkassen et al. (1995), Eidel and Fischer (2018) and Fish (2014). We assume that the system is composed of two different periodically distributed[2] linear elastic materials, in which a unit reference cell of volume $\mathcal{V}$ is periodically repeated covering the macroscopic domain. Let $\boldsymbol{F}^\epsilon(^M\boldsymbol{x}) = \boldsymbol{F}(^M\boldsymbol{x}, \boldsymbol{x})$ denote a generic tensor-valued function which is $\mathcal{V}-$periodic in $\boldsymbol{x}$ over the unit cell $\mathcal{V}$ and which features slow (with $^M\boldsymbol{x}$) and fast (with $\boldsymbol{x}$) variations. Hence, we have

$$\nabla_{^M\boldsymbol{x}} \boldsymbol{F}^\epsilon(^M\boldsymbol{x}) = \nabla_{^M\boldsymbol{x}} \boldsymbol{F}(^M\boldsymbol{x}, \boldsymbol{x}) + \frac{1}{\epsilon}\nabla_{\boldsymbol{x}} \boldsymbol{F}(^M\boldsymbol{x}, \boldsymbol{x}), \tag{5}$$

$$\text{div}_{^M\boldsymbol{x}} \boldsymbol{F}^\epsilon(^M\boldsymbol{x}) = \text{div}_{^M\boldsymbol{x}} \boldsymbol{F}(^M\boldsymbol{x}, \boldsymbol{x}) + \frac{1}{\epsilon}\text{div}_{\boldsymbol{x}} \boldsymbol{F}(^M\boldsymbol{x}, \boldsymbol{x}). \tag{6}$$

In a heterogeneous body under applied loads, examples of such multi-scale functions are the displacements $\boldsymbol{u}^\epsilon$, strains $\boldsymbol{\varepsilon}^\epsilon$ and stresses $\boldsymbol{\sigma}^\epsilon$, which we write as

$$\boldsymbol{u}^\epsilon(^M\boldsymbol{x}) = \boldsymbol{u}(^M\boldsymbol{x}, \boldsymbol{x}), \tag{7}$$

$$\boldsymbol{\varepsilon}^\epsilon(^M\boldsymbol{x}) = \boldsymbol{\varepsilon}(^M\boldsymbol{x}, \boldsymbol{x}), \tag{8}$$

$$\boldsymbol{\sigma}^\epsilon(^M\boldsymbol{x}) = \boldsymbol{\sigma}(^M\boldsymbol{x}, \boldsymbol{x}). \tag{9}$$

For convenience, a third domain, $\mathcal{B}^\epsilon$, which is referred to as the composite domain, is introduced (Fish, 2014). Here, ϵ reflects the presence of fine-scale features, e.g., unlike the macroscale domain boundary $\partial\mathcal{B}$, the composite domain boundary $\partial\mathcal{B}^\epsilon$ may be rough at the fine-scale. The equilibrium equation of elastomechanics at the composite domain, assuming vanishing body forces, is given by

$$\boldsymbol{0} = \text{div}_{^M\boldsymbol{x}} \boldsymbol{\sigma}^\epsilon \quad \text{in } \mathcal{B}^\epsilon. \tag{10}$$

On the other hand, by assuming infinitesimal and linear elasticity we have the following stress description

$$\boldsymbol{\sigma}^\epsilon = \mathbb{C}^\epsilon : \boldsymbol{\varepsilon}^\epsilon \quad \text{in } \mathcal{B}^\epsilon. \tag{11}$$

In general $\mathbb{C}^\epsilon = \mathbb{C}(^M\boldsymbol{x}, \boldsymbol{x})$ where the constitutive tensor $\mathbb{C}$ is $\mathcal{V}-$periodic in $\boldsymbol{x}$ over the unit cell $\mathcal{V}$ and it shows slow as well as fast variations. For simplicity, we disregard its slow variation and directional dependence and assume that $\mathbb{C}^\epsilon = \mathbb{C}(\boldsymbol{x})$ with $\mathbb{C}_i = 3K_i \mathbb{I}^{\text{vol}} + 2G_i \mathbb{I}^{\text{dev}}$ where $\mathbb{I}^{\text{vol}} = 1/3\boldsymbol{1} \otimes \boldsymbol{1}$, and $\mathbb{I}^{\text{dev}} = \mathbb{I} - \mathbb{I}^{\text{vol}}$ with $\mathbb{I} = 1/2[\boldsymbol{1} \overline{\otimes} \boldsymbol{1} + \boldsymbol{1} \underline{\otimes} \boldsymbol{1}]$. Here, K_i and G_i are bulk and shear moduli associated with phase i, respectively, and $\boldsymbol{1}$ is the second-order identity tensor. The $\mathcal{V}-$periodic compliance tensor $\mathbb{S}$ is defined as $\mathbb{S} = \mathbb{C}^{-1}$. The following definition is valid for strain $\boldsymbol{\varepsilon}^\epsilon$

$$\boldsymbol{\varepsilon}^\epsilon = \text{sym}\left(\nabla_{^M\boldsymbol{x}} \boldsymbol{u}^\epsilon\right) \quad \text{in } \mathcal{B}^\epsilon. \tag{12}$$

Finally, Eqs. (10)–(12) are subject to the prescribed boundary displacements and tractions with $\boldsymbol{u}^\epsilon = \overline{\boldsymbol{u}}^\epsilon$ on $\partial\mathcal{B}_{\boldsymbol{u}}^\epsilon$ and $\boldsymbol{\sigma}^\epsilon \cdot \boldsymbol{n}^\epsilon = \overline{\boldsymbol{t}}^\epsilon$ on $\partial\mathcal{B}_{\boldsymbol{t}}^\epsilon$, respectively. $\boldsymbol{n}^\epsilon$ is the unit normal to the surface at which the traction is computed. Here, considering that $\partial\mathcal{B}^\epsilon$ is the boundary of the composite domain $\mathcal{B}^\epsilon$, $\partial\mathcal{B}_{\boldsymbol{u}}^\epsilon$ and $\partial\mathcal{B}_{\boldsymbol{t}}^\epsilon$ respectively denote the boundary parts subjected to prescribed displacements and tractions with $\partial\mathcal{B}_{\boldsymbol{u}}^\epsilon \bigcap \partial\mathcal{B}_{\boldsymbol{t}}^\epsilon = \varnothing$ and $\partial\mathcal{B}_{\boldsymbol{u}}^\epsilon \bigcup \partial\mathcal{B}_{\boldsymbol{t}}^\epsilon = \partial\mathcal{B}^\epsilon$.

We now apply a two-scale asymptotic expansion of the solution $\boldsymbol{u}^\epsilon(^M\boldsymbol{x})$ in terms of the fast and slow coordinates

$$\boldsymbol{u}^\epsilon(^M\boldsymbol{x}) = \boldsymbol{u}^{(0)}(^M\boldsymbol{x}, \boldsymbol{x}) + \epsilon\boldsymbol{u}^{(1)}(^M\boldsymbol{x}, \boldsymbol{x}) + \epsilon^2\boldsymbol{u}^{(2)}(^M\boldsymbol{x}, \boldsymbol{x}) + O(\epsilon^3), \tag{13}$$

where $\boldsymbol{u}^{(i)}$ are $\mathcal{V}-$periodic functions in $\boldsymbol{x}$. The leading order $\boldsymbol{u}^{(0)}$

---

[2] Even if the microstructure is not periodic, the response functions and the solutions are assumed to be so.

corresponds to the homogenized displacement field, and as is shown below, it only depends on the macroscopic coordinates $^M\boldsymbol{x}$, i.e., it is constant over the unit cell domain. Putting the above ansatz into Eqs. (11)–(13) we obtain the following expansions for $\boldsymbol{\varepsilon}^\epsilon$ and $\boldsymbol{\sigma}^\epsilon$

$$\boldsymbol{\varepsilon}^\epsilon(^M\boldsymbol{x}) = \frac{1}{\epsilon}\boldsymbol{\varepsilon}^{(-1)}(^M\boldsymbol{x}, \boldsymbol{x}) + \boldsymbol{\varepsilon}^{(0)}(^M\boldsymbol{x}, \boldsymbol{x}) + \epsilon\,\boldsymbol{\varepsilon}^{(1)}(^M\boldsymbol{x}, \boldsymbol{x}) + \epsilon^2\boldsymbol{\varepsilon}^{(2)}(^M\boldsymbol{x}, \boldsymbol{x})$$
$$+ O(\epsilon^3), \tag{14}$$

$$\boldsymbol{\sigma}^\epsilon(^M\boldsymbol{x}) = \frac{1}{\epsilon}\boldsymbol{\sigma}^{(-1)}(^M\boldsymbol{x}, \boldsymbol{x}) + \boldsymbol{\sigma}^{(0)}(^M\boldsymbol{x}, \boldsymbol{x}) + \epsilon\,\boldsymbol{\sigma}^{(1)}(^M\boldsymbol{x}, \boldsymbol{x}) + \epsilon^2\boldsymbol{\sigma}^{(2)}(^M\boldsymbol{x}, \boldsymbol{x})$$
$$+ O(\epsilon^3), \tag{15}$$

where we have defined the quantities

$$\boldsymbol{\varepsilon}^{(-1)} = \mathrm{sym}(\nabla_{\boldsymbol{x}}\boldsymbol{u}^{(0)}) \quad \text{and} \quad \boldsymbol{\varepsilon}^{(k)} = \boldsymbol{\varepsilon}^{(k)}_{\langle^M\boldsymbol{x}\rangle} + \boldsymbol{\varepsilon}^{(k+1)}_{\langle\boldsymbol{x}\rangle} \quad \text{for } k \geq 0 \tag{16}$$

with

$$\boldsymbol{\varepsilon}^{(k)}_{\langle^M\boldsymbol{x}\rangle} = \mathrm{sym}\left(\nabla_{^M\boldsymbol{x}}\boldsymbol{u}^{(k)}\right) \quad \text{and} \quad \boldsymbol{\varepsilon}^{(k)}_{\langle\boldsymbol{x}\rangle} = \mathrm{sym}(\nabla_{\boldsymbol{x}}\boldsymbol{u}^{(k)}). \tag{17}$$

Using Eq. (11) the quantities $\boldsymbol{\sigma}^{(k)}$ and $\boldsymbol{\varepsilon}^{(k)}$ are then related by the following elastic constitutive relation

$$\boldsymbol{\sigma}^{(k)} = \mathbb{C} : \boldsymbol{\varepsilon}^{(k)} \quad \text{for } k \geq -1. \tag{18}$$

We substitute now the asymptotic expansion for the stress tensor, Eq. (15), into the equilibrium Eq. (10), and comparing coefficients of different powers in ϵ we obtain

$$O(\epsilon^{-2}): \quad \boldsymbol{0} = \mathrm{div}_{\boldsymbol{x}}\boldsymbol{\sigma}^{(-1)}, \tag{19}$$

$$O(\epsilon^{-1}): \quad \boldsymbol{0} = \mathrm{div}_{^M\boldsymbol{x}}\boldsymbol{\sigma}^{(-1)} + \mathrm{div}_{\boldsymbol{x}}\boldsymbol{\sigma}^{(0)}, \tag{20}$$

$$O(\epsilon^0): \quad \boldsymbol{0} = \mathrm{div}_{^M\boldsymbol{x}}\boldsymbol{\sigma}^{(0)} + \mathrm{div}_{\boldsymbol{x}}\boldsymbol{\sigma}^{(1)}. \tag{21}$$

Since $\mathbb{C}$ depends only on the microscopic variables, and rewriting Eq. (19) as

$$\mathrm{div}_{\boldsymbol{x}}[\mathbb{C} : \mathrm{sym}(\nabla_{\boldsymbol{x}}\boldsymbol{u}^{(0)})] = \boldsymbol{0}, \tag{22}$$

we can conclude that $\boldsymbol{u}^{(0)} = \boldsymbol{u}^{(0)}(^M\boldsymbol{x})$, that is, $\boldsymbol{u}^{(0)}$ is expressed only in terms of macroscopic coordinates, as mentioned above, and so is $\boldsymbol{\varepsilon}^{(0)}_{\langle^M\boldsymbol{x}\rangle}(^M\boldsymbol{x})$. In addition, and considering Eqs. (16) and (18), we have $\boldsymbol{\varepsilon}^{(-1)} = \boldsymbol{\sigma}^{(-1)} = \boldsymbol{0}$. This shows that the leading orders of the stress and strain tensors are $\boldsymbol{\varepsilon}^{(0)}$ and $\boldsymbol{\sigma}^{(0)}$, respectively. The goal now is to find a homogenised (macroscopic) equation for $\boldsymbol{u}^{(0)}$ that is written in terms of the homogenised (macroscopic) strain tensor $\boldsymbol{\varepsilon}^{(0)}_{\langle^M\boldsymbol{x}\rangle}$.

Since $\boldsymbol{\sigma}^{(-1)} = \boldsymbol{0}$, Eq. (20) becomes $\mathrm{div}_{\boldsymbol{x}}\boldsymbol{\sigma}^{(0)} = \boldsymbol{0}$, which, using Eq. (16), can be rewritten as

$$\mathrm{div}_{\boldsymbol{x}}(\mathbb{C} : \boldsymbol{\varepsilon}^{(1)}_{\langle\boldsymbol{x}\rangle}) = -\mathrm{div}_{\boldsymbol{x}}\left(\mathbb{C} : \boldsymbol{\varepsilon}^{(0)}_{\langle^M\boldsymbol{x}\rangle}\right). \tag{23}$$

The right-hand side of the above equation is the product between a function that depends on the microscopic variables only ($\mathbb{C}$) and a function that the depends on the macroscopic variables only ($\boldsymbol{\varepsilon}^{(0)}_{\langle^M\boldsymbol{x}\rangle}$). Therefore, to solve $\boldsymbol{u}^{(1)}$ up to a constant, we apply separation of variables and consider solutions of the form $\boldsymbol{u}^{(1)}(^M\boldsymbol{x}, \boldsymbol{x}) = \boldsymbol{\chi}^{mn}(\boldsymbol{x})\varepsilon^{(0)}_{\langle^M\boldsymbol{x}\rangle,mn}$. Thus, we have

$$\boldsymbol{\varepsilon}^{(1)}_{\langle\boldsymbol{x}\rangle} = \mathrm{sym}(\nabla_{\boldsymbol{x}}\boldsymbol{\chi}^{mn})\varepsilon^{(0)}_{\langle^M\boldsymbol{x}\rangle,mn}. \tag{24}$$

Here, $\boldsymbol{\chi}^{mn}(\boldsymbol{x})$ is a $\mathcal{V}-$periodic C^0 continuous, vector-valued first-order displacement influence function, also known as a corrector function, with symmetry $\boldsymbol{\chi}^{mn}(\boldsymbol{x}) = \boldsymbol{\chi}^{nm}(\boldsymbol{x})$ for $m, n = 1, 2, 3$. Moreover, $\mathcal{V}-$periodicity of $\boldsymbol{\chi}^{mn}(\boldsymbol{x})$ renders the following integration over the unit cell

$$\int_{\mathcal{V}} \nabla_{\boldsymbol{x}}\boldsymbol{\chi}^{mn}\mathrm{d}V = \boldsymbol{0} \text{ for } m, n = 1, 2, 3. \tag{25}$$

Putting the ansatz for $\boldsymbol{\varepsilon}^{(1)}_{\langle\boldsymbol{x}\rangle}$ given in Eq. (24) into Eq. (23) and considering the validity of Eq. (23) for arbitrary macroscopic strains $\boldsymbol{\varepsilon}^{(0)}_{\langle^M\boldsymbol{x}\rangle}$

along with using the minor symmetry of $\mathbb{C}^\epsilon$ which provides $C_{ijkl} = C_{ijlk} = C_{jikl} = C_{jilk}$ with $C_{ijkl} = [\boldsymbol{e}_i \otimes \boldsymbol{e}_j] : \mathbb{C} : [\boldsymbol{e}_k \otimes \boldsymbol{e}_l]$ we obtain the following cell problem

$$-\frac{\partial}{\partial x_j}\left[C_{ijkl}\frac{\partial\chi_k^{mn}(\boldsymbol{x})}{\partial x_l}\right] = \frac{\partial C_{ijmn}}{\partial x_j} \quad \text{in} \quad \mathcal{V} = \mathcal{B}_1 \cup \mathcal{B}_2. \tag{26}$$

Together with locally periodic boundary conditions, Eq. (26) is a linear boundary value problem for $\boldsymbol{\chi}^{nm}(\boldsymbol{x})$ up to a constant. The function $\boldsymbol{\chi}^{lm}(\boldsymbol{x})$, which is a solution of the cell problem (26), provides information of the microscopic details of the system, and as such, it is a key quantity of the homogenised problem.

We can write the leading order (fine scale) strain tensor $\boldsymbol{\varepsilon}^{(0)}(^M\boldsymbol{x}, \boldsymbol{x}) = \boldsymbol{\varepsilon}^{(0)}_{\langle^M\boldsymbol{x}\rangle} + \boldsymbol{\varepsilon}^{(1)}_{\langle\boldsymbol{x}\rangle}$ in the following separated form

$$\varepsilon_{kl}^{(0)} = \mathcal{E}_{kl}^{mn}(\boldsymbol{x})\varepsilon^{(0)}_{\langle^M\boldsymbol{x}\rangle,mn} \quad \text{with} \quad \mathcal{E}_{kl}^{mn}(\boldsymbol{x})$$
$$= \mathcal{I}_{klmn} + \frac{1}{2}\left[\frac{\partial\chi_k^{mn}(\boldsymbol{x})}{\partial x_l} + \frac{\partial\chi_l^{mn}(\boldsymbol{x})}{\partial x_k}\right], \tag{27}$$

where $\mathcal{E}_{kl}^{mn}(\boldsymbol{x})$ is the strain influence function. $\mathcal{I}_{klmn} = 1/2[\delta_{km}\delta_{\mathrm{ln}} + \delta_{kn}\delta_{lm}]$ for $k, l, m, n = 1, 2, 3$ are the components of the fourth-order symmetric identity tensor. This shows, in view of Eqs. (18) and (27), that the leading order (fine scale) stress tensor $\boldsymbol{\sigma}^{(0)}(^M\boldsymbol{x}, \boldsymbol{x})$ depends only on the corrector function $\boldsymbol{\chi}^{lm}(\boldsymbol{x})$ and the macroscopic strain tensor $\boldsymbol{\varepsilon}^{(0)}_{\langle^M\boldsymbol{x}\rangle}$ with

$$\sigma_{ij}^{(0)} = \mathcal{S}_{ij}^{mn}(\boldsymbol{x})\varepsilon^{(0)}_{\langle^M\boldsymbol{x}\rangle,mn}$$
$$\text{with} \quad \mathcal{S}_{ij}^{mn}(\boldsymbol{x}) = C_{ijkl}(\boldsymbol{x})\mathcal{E}_{kl}^{mn}(\boldsymbol{x}) = C_{ijmn} + C_{ijkl}\frac{\partial\chi_k^{mn}(\boldsymbol{x})}{\partial x_l}, \tag{28}$$

where $\mathcal{S}_{ij}^{mn}(\boldsymbol{x})$ is the stress influence function. Making use of the divergence theorem and the fact that $\boldsymbol{\sigma}^{(1)}$ is periodic in $\mathcal{V}$, we have $\int_{\mathcal{V}} \mathrm{div}_{\boldsymbol{x}}\boldsymbol{\sigma}^{(1)}\mathrm{d}V = \int_{\partial\mathcal{V}} \boldsymbol{\sigma}^{(1)}\cdot\boldsymbol{n}\mathrm{d}A = \boldsymbol{0}$. Thus, integrating Eq. (21) over the unit cell, we obtain

$$\frac{1}{|\mathcal{V}|}\int_{\mathcal{V}}\left[\mathrm{div}_{^M\boldsymbol{x}}\boldsymbol{\sigma}^{(0)} + \mathrm{div}_{\boldsymbol{x}}\boldsymbol{\sigma}^{(1)}\right]\mathrm{d}V = \mathrm{div}_{^M\boldsymbol{x}}\left(\frac{1}{|\mathcal{V}|}\int_{\mathcal{V}}\boldsymbol{\sigma}^{(0)}\mathrm{d}V\right)$$
$$= \mathrm{div}_{^M\boldsymbol{x}}{}^M\boldsymbol{\sigma} = \boldsymbol{0}. \tag{29}$$

This is the (macroscopic) homogenized equilibrium equation where the volume averaged stress tensor $^M\boldsymbol{\sigma}$ reads

$$^M\boldsymbol{\sigma} = \frac{1}{|\mathcal{V}|}\int_{\mathcal{V}}\boldsymbol{\sigma}^{(0)}\mathrm{d}V. \tag{30}$$

Analogously to Eq. (30), volume averaged strain tensor $^M\boldsymbol{\varepsilon}$ can be computed through an averaging of $\boldsymbol{\varepsilon}^{(0)}$ over the unit cell

$$^M\boldsymbol{\varepsilon} = \frac{1}{|\mathcal{V}|}\int_{\mathcal{V}}\boldsymbol{\varepsilon}^{(0)}\mathrm{d}V. \tag{31}$$

In view of Eqs. (25) and (27), one computes $^M\boldsymbol{\varepsilon} = \boldsymbol{\varepsilon}^{(0)}_{\langle^M\boldsymbol{x}\rangle}$. Substituting Eq. (28) into the right-hand side of Eq. (30) yields the following macroscale constitutive equation

$$^M\boldsymbol{\sigma} = \mathbb{C}^\star : {}^M\boldsymbol{\varepsilon}, \tag{32}$$

where $\mathbb{C}^\star$ is the macroscopic elastic stiffness tensor with

$$C_{ijmn}^\star = \frac{1}{|\mathcal{V}|}\int_{\mathcal{V}}\mathcal{S}_{ij}^{mn}(\boldsymbol{x})\mathrm{d}V. \tag{33}$$

$\mathbb{C}^\star$ possesses both major and minor symmetries as does $\mathbb{C}$. For derivation of the components of the macroscopic elasticity tensor $\mathbb{C}^\star$, we represent the unit cell problem given in Eq. (26) in terms of the so-called *total* displacement influence function $\boldsymbol{\psi}^{mn} = \boldsymbol{\chi}^{mn} + \boldsymbol{\varpi}^{mn}$ where $\varpi_k^{mn} = x_n\delta_{km}$ which gives

$$\frac{\partial}{\partial x_j}\left[C_{ijkl}\frac{\partial\psi_k^{mn}(\boldsymbol{x})}{\partial x_l}\right] = 0 \quad \text{in} \quad \mathcal{V} = \mathcal{B}_1 \cup \mathcal{B}_2. \tag{34}$$

Analogous to Eq. (26), together with locally periodic boundary conditions, Eq. (34) is a linear boundary value problem for $\boldsymbol{\psi}^{nm}(\boldsymbol{x})$ up to a
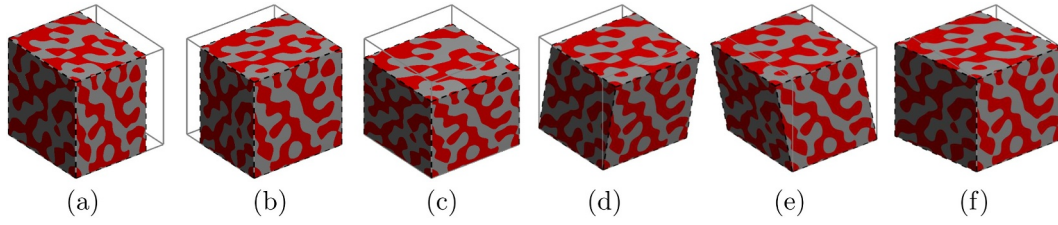
Fig. 3. Considering that the problem is a linear one, and in order to provide stress and strain distributions over the unit cell with reasonable magnitudes, we apply small macroscopic strains with six homogeneous deformation fields corresponding to $\alpha \varpi_k^{mn}$ for $mn = 11, 22, 33, 23, 13, 12$. These yield macroscopic strains of $^M\varepsilon(\alpha\varpi^{mn}) = \alpha \, ^M\varepsilon(\varpi_k^{mn})$ where $^M\varepsilon(\varpi^{11}) = e_1 \otimes e_1$, $^M\varepsilon(\varpi^{22}) = e_2 \otimes e_2$, $^M\varepsilon(\varpi^{33}) = e_3 \otimes e_3$, $^M\varepsilon(\varpi^{23}) = 1/2[e_2 \otimes e_3 + e_3 \otimes e_2]$, $^M\varepsilon(\varpi^{13}) = 1/2[e_1 \otimes e_3 + e_3 \otimes e_1]$, $^M\varepsilon(\varpi^{12}) = 1/2[e_1 \otimes e_2 + e_2 \otimes e_1]$ and $\alpha = -0.001$. The $\mathcal{V}-$periodic fluctuation field χ^{mn}, which is not displayed above, has no influence on the emergent macroscopic strains. The grey box represents the undeformed volume element contours whereas the dashed curves convect with the deformation. For visibility purposes the displacements are amplified.

constant. To provide uniqueness, a common approach used is to set $\psi^{nm}(x) = \varpi^{nm}(x)$, i.e., $\chi^{nm}(x) = 0$, on the vertices of the unit cell, which constitute control nodes used to impose macroscropic strains.

Substituting the representation $\chi^{mn} = \psi^{mn} - \varpi^{mn}$ into the strain influence function given in Eq. (27) with the definition $\varpi_k^{mn} = x_n \delta_{km}$ we reach

$$
\begin{aligned}
\mathcal{E}_{kl}^{mn}(x) &= \mathcal{I}_{klmn} + \frac{1}{2}\left[\frac{\partial[\psi_k^{mn}(x) - \varpi_k^{mn}(x)]}{\partial x_l} + \frac{[\psi_l^{mn}(x) - \varpi_l^{mn}(x)]}{\partial x_k} \right], \\
&= \mathcal{I}_{klmn} - \mathcal{I}_{klmn} + \frac{1}{2}\left[\frac{\partial\psi_k^{mn}(x)}{\partial x_l} + \frac{\psi_l^{mn}(x)}{\partial x_k} \right], \\
&= \frac{1}{2}\left[\frac{\partial\psi_k^{mn}(x)}{\partial x_l} + \frac{\psi_l^{mn}(x)}{\partial x_k} \right].
\end{aligned}
\tag{35}
$$

Considering the unitary character macroscopic strain due to *total* displacement influence function ψ^{mn} for each mn-pair, we may define $\mathcal{E}_{kl}^{mn}(x)$ as the microscopic strain components due to total displacement influence function ψ^{mn} with $\mathcal{E}_{kl}^{mn}(x) = \varepsilon_{kl}^{(0)}(\psi^{mn})$. Similarly, in view of Eq. (28), $\mathcal{S}_{kl}^{mn}(x)$ is interpreted as the microscopic stress components due to the *total* displacement influence function ψ^{mn} with $\mathcal{S}_{kl}^{mn}(x) = \sigma_{kl}^{(0)}(\psi^{mn})$. Substituting this into Eq. (33), we find

$$
C_{ijmn}^\star = \frac{1}{|\mathcal{V}|} \int_\mathcal{V} \sigma_{kl}^{(0)}(\psi^{mn}) \mathrm{d}V .
\tag{36}
$$

In words, the component of the macroscopic elasticity tensor $\mathbb{C}^\star$ with the indices $ijmn$ corresponds to the homogenized stress tensor component $^M\sigma_{ij}$ for due to *total* displacement influence function ψ^{mn} computed for the imposed macroscropic strains at unit cell vertices with ϖ_k^{mn}. Thus, computation of the 36 macroscopic constitutive constants making up $C_{ijmn}^\star$ requires computation of the homogenized stress $^M\sigma$ for six load cases with $mn = 11, 22, 33, 23, 13, 12$, see Fig. 3. For convenience, in the following pages we denote $\varepsilon^{(0)}$ and $\sigma^{(0)}$ with ε and σ, respectively. The results listed above for periodic microstructures, are valid even if the material is random and not periodic as in the current case.[3]

For completeness, we close this part by presenting the boundary value problem at the macroscale domain $\mathcal{B}$. For vanishing body forces, this aims at finding the macroscale displacement field $^M u = u^{(0)}(^M x)$ on $\mathcal{B}$ such that

$$
0 = \mathrm{div}_{M_x} {}^M\sigma \quad \text{in } \mathcal{B} .
\tag{37}
$$

Eq. (37) with $^M\sigma$ computed in view of Eq. (32) are subject to the prescribed boundary displacements and tractions with $^M u = {}^M \bar{u}$ on $\partial\mathcal{B}_u$ and $^M\sigma \cdot {}^M n = {}^M \bar{t}$ on $\partial\mathcal{B}_t$, respectively. $^M n$ is the unit normal to the surface at which the traction is computed. Here, considering that $\partial\mathcal{B}$ is the boundary of the domain $\mathcal{B}$, $\partial\mathcal{B}_u$ and $\partial\mathcal{B}_t$ respectively denote the boundary parts subjected to prescribed displacements and tractions

with $\partial\mathcal{B}_u \bigcap \partial\mathcal{B}_t = \varnothing$ and $\partial\mathcal{B}_u \bigcup \partial\mathcal{B}_t = \partial\mathcal{B}$.

2.3. Boundary conditions

During the application of the different load cases, we subject the representative volume boundaries to two different boundary conditions each of which results in a periodic deformation of the unit cell, in accordance with the outlined asymptotic homogenization based macroscopic property definition scheme. These are periodic boundary conditions (PBC) and kinematic uniform boundary conditions (KUBC), both of which are applied under displacement control and for which the equivalence of average microscopic stress power to the macroscopic stress power (Hill, 1972) is a priori satisfied (Miehe and Koch, 2002). We consider periodic boundary conditions by taking both periodic deformations and antiperiodic tractions as

$$
\begin{aligned}
u(x^+, t) - u(x^-, t) &= {}^M d(t) \cdot [x^+ - x^-], \\
t(x^+, t) + t(x^-, t) &= 0 .
\end{aligned}
\tag{38}
$$

Here, $^M d$ is the macroscopic displacement gradient yielding $^M\varepsilon = \mathrm{sym}(^M d)$. Moreover, $x^+ \in \partial\mathcal{V}^+$ and $x^- \in \partial\mathcal{V}^-$ correspond to two material points periodically located at the representative volume boundary with outward normals n^+ and n^-, respectively, which satisfy $n^+ = -n^-$. On the other hand, considering that $\partial\mathcal{V}$ corresponds to the representative volume boundary, kinematic uniform boundary conditions are defined by taking displacements that comply with the assigned macroscopic strains on $\partial\mathcal{V}$

$$
u(x, t) = {}^M d(t) \cdot x \quad \forall \; x \in \partial\mathcal{V} ,
\tag{39}
$$

Thus, kinematic uniform boundary conditions correspond to a special case of periodic boundary conditions where the perturbation field vanishes on $\partial\mathcal{V}$.

A third type of boundary condition, referred to as uniform traction condition (UTBC), is defined via tractions that comply with the assigned macroscopic stresses $t(x, t) = {}^M\sigma(t) \cdot n$. This boundary condition is applied under force control to yield the apparent compliance tensor. Denoting elastic stiffness tensors obtained by using periodic, kinematic uniform and uniform traction boundary conditions by $\mathbb{C}_{PBC}$, $\mathbb{C}_{KUBC}$ and $\mathbb{C}_{UTBC}$, respectively, the homogenization results derived by Suquet (1987) yield the following universal inequality

$$
^M\varepsilon : \mathbb{C}_{UTBC}^\star : {}^M\varepsilon \leq {}^M\varepsilon : \mathbb{C}_{PBC}^\star : {}^M\varepsilon \leq {}^M\varepsilon : \mathbb{C}_{KUBC}^\star : {}^M\varepsilon .
\tag{40}
$$

Thus, the macroscopic elastic stiffness predictions of kinematic uniform and uniform traction boundary conditions respectively correspond to an upper and lower bound on the macroscoic stiffness. Therefore, the use of periodic boundary conditions for the computations of the elastic properties is a more reasonable approach.

---

[3] At the expense of doubling the size of the volume element, periodization of the microstructure is possible using a mirroring operation (Pahr and Zysset, 2008).

3. Results and discussions

3.1. Determination of the RVE size

Effective properties inherently assume the existence of an RVE, a concept on which continuum mechanics relies (Ostoja-Starzewski et al., 2016). Unit cells making up periodic media and volume elements of very large sizes (mathematically tending to infinity), which encapsulate sufficient microstructural information and that feature statistical homogeneous ergodic properties, qualify as RVEs (Ostoja-Starzewski, 2007; Torquato, 2002). In the current paper, we apply homogenization by systematically increasing the generated volume element size and investigate the convergence of homogenized apparent elastic properties. To this end, we consider periodic boundary conditions.

For the elastic moduli of polycrystals, i.e. aggregate of single crystals, randomly distributed orientations of single crystals lead to macroscopically isotropic properties. For polycrystalline materials, considering that the aggregate of crystals occupy the whole volume, the Voigt and Reuss averages correspond to directional averages considering all possible lattice orientations, with

$$\mathbb{C}_V = \frac{1}{4\pi} \int_0^{2\pi} \int_0^{\pi} \mathbb{C}(\Theta, \Phi) \sin \Theta \, d\Theta \, d\Phi \quad \text{and}$$

$$\mathbb{S}_R = \frac{1}{4\pi} \int_0^{2\pi} \int_0^{\pi} \mathbb{S}(\Theta, \Phi) \sin \Theta \, d\Theta \, d\Phi, \tag{41}$$

which are fourth-order stiffness and compliance tensors, respectively. Since both $\mathbb{C}_V$ and $\mathbb{S}_R$ are isotropic we can describe them in terms of K_V, G_V and K_R, G_R, respectively.

Similar to the case of polycrystals, the generated bicontinuous stochastic composite microstructures feature macroscopically isotropic elastic properties only for sufficiently large volume element sizes, otherwise a strong directional dependence may be observed in the macroscopic elasticity tensor. Due to the randomness in the generation of the microstructures, computation of elastic properties for only one selected direction may be misleading. Therefore, we treat the macroscopic elasticity tensor of each volume element as that of a single crystal making up a crystalline aggregate by using the substitution of the macroscopic elasticity and compliance tensors, $\mathbb{C}^\star$ and $\mathbb{S}^\star$, respectively, in the integrands of Eq. (41). This allows demonstrating macroscopic elastic properties with a single parameter, namely Hill's aggregate elastic properties, $K_{HVR}^\star = [K_V^\star + K_R^\star]/2$ and $G_{HVR}^\star = [G_V^\star + G_R^\star]/2$, (Hill, 1952). Moreover, this allows quantifying the level of anisotropy in the material using the macroscopic universal anisotropy index $A_U^\star$ (Ranganathan and Ostoja-Starzewski, 2008), with $A_U^\star = K_V^\star/K_R^\star + 5G_V^\star/G_R^\star - 6 \geq 0$. $A_U^\star$ increases with increasing level of anisotropy. As the medium converges to an isotropic one, the gap in-between Voigt and Reuss bounds vanishes with $K_V^\star \to K_R^\star$ and $G_V^\star \to G_R^\star$. This amounts to $A_U^\star = 0$. Corresponding Young's moduli and Poisson's ratios are computed with $E_{HVR}^\star = 9K_{HVR}^\star G_{HVR}^\star/[3K_{HVR}^\star + G_{HVR}^\star]$ and $\nu_{HVR}^\star = [1/2][3K_{HVR}^\star - 2G_{HVR}^\star]/[3K_{HVR}^\star + G_{HVR}^\star]$, respectively. Once the effective properties are concerned, the subscript HVR is dropped.

In the definition of the RVE size, model generations for various volume element sizes are considered as demonstrated in Fig. 4. A two-phase elastic nanocomposite, with constituent phase contrast corresponding to $E_2/E_1 = 1$, is homogeneous and any material volume, no matter how small its size is, encapsulates the macroscopic properties. Thus, one deduces that a phase contrast of $E_2/E_1 = 0$ constitutes the most stringent condition for a minimum RVE size which is computationally detected. With this motivation, in this part of our work, we consider single phase gold with phase contrast of $E_2/E_1 = 0$, where E_1 and E_2, respectively denote Young's modulus of gold and pore. Taking into account the experimentally observed phase volume fraction interval in nanoporous gold, phase volume fractions of $\phi_1 = 0.20$ and 0.50 are studied. For the single gold phase, we assume isotropic elasticity and use $E_1 = 79$ GPa and $\nu_1 = 0.44$. All of the reported results on the subsequent pages constitute averages of those corresponding to five

stochastic realizations using the leveled-wave model, as defined by Eq. (2). As shown in the subsequent results, for the determined RVE size the standard deviation in the computed effective properties from the five stochastic realizations is sufficiently small. In each realization, $N = 10,000$ waves are used which is sufficient to guarantee Gaussian statistical properties of the random field $f(x)$. We use 3D full integration first order trilinear finite elements carried out of voxelization of the generated domain where the voxels are dimensionless and unit-sized. In absence of consideration of any size dependent constitutive phenomena, the computed mechanical properties are equally valid for any microstructural size.

The volume element size dependence of the computed apparent elastic properties, more specifically bulk modulus $K^\star$, shear modulus $G^\star$ and Poisson's ratio $\nu^\star$ are given in Fig. 5 for the solid phase volume fractions of 0.20 and 0.50. Results are also tabulated in Tables B.1 and B.2. As anticipated, a fast convergence of the mean elastic properties with increased volume element size is observed with the use of periodic boundary conditions. During this convergence of mean values, corresponding error bars get smaller. The mean anisotropy index $A_U^\star$ of both volume fractions decrease swiftly with increasing volume element size, which signals isotropicization. Depending on the computed relative errors (cf. Tables B.1 and B.2) and considering the computational resources, the minimum RVE size is judged to be 12 wavelengths and it is used in all of the subsequent investigations. At this size, for 0.20 of phase volume fraction, $K^\star$, $G^\star$ and $\nu^\star$ are computed as 32.92 ± 7.72 MPa, 27.49 ± 6.88 MPa and 0.1654 ± 0.0180, respectively. Moreover, the effective anisotropy index is computed to be $A_U^\star = 2.27 \times 10^{-1}$. For 0.50 of phase volume fraction, on the other hand, $K^\star$, $G^\star$ and $\nu^\star$ are computed as 10915.24 ± 176.32 MPa, 5588.84 ± 66.48 MPa and 0.2813 ± 0.0009. Also, the effective anisotropy index is computed to be $A_U^\star = 2.21 \times 10^{-2}$, cf. (Soyarslan et al., 2018b). As the effective bulk and shear moduli are concerned, these predictions are much below the upper bounds computed by Hashin–Shtrikman, three-point Beran-Molyneux and Milton-Phan-Tien bounds. The bounds for 0.20 gold volume fraction are $K_{U,HS} = 7567.05$ MPa, $G_{U,HS} = 3428.82$ MPa, $[K_{U,BM,I} + K_{U,BM,II}]/2 = 1935.43$ MPa, and $[G_{U,MPT,I} + G_{U,MPT,II}]/2 = 1484.50$ MPa. The bounds for 0.50 gold volume fraction are $K_{U,HS} = 27430.56$ MPa, $G_{U,HS} = 9974.75$ MPa, $[K_{U,BM,I} + K_{U,BM,II}]/2 = 15647.72$ MPa, and $[G_{U,MPT,I} + G_{U,MPT,II}]/2 = 7831.89$ MPa (cf. Tables B.1 and B.2). The bounds get closer to the computed values with increasing solid volume fraction.

3.2. The influence of material property contrast

Based on the determined RVE size, we demonstrate the influences of phase contrast on the effective elastic properties of the composite. To this end, fixing E_1 to the elasticity modulus of gold with $E_1 = 79$ GPa, four phase contrast values, in terms of elasticity moduli ratio $E_2/E_1 = \{10^{-4}, 10^{-3}, 10^{-2}, 10^{-1}\}$ are considered. $E_2/E_1 = 1$ corresponds to the trivial case of a homogeneous material and does not require any computations. $E_2/E_1 = 0$ corresponds to a porous solid for which the results are reported in the previous section.

Figs. 6 and 7 demonstrate deformed shapes of the volume elements as well as strain and stress contours for $E_2/E_1 = 10^{-4}$ and $E_2/E_1 = 10^{-1}$, respectively, considering $\phi_1 \simeq 0.20$. Here, the six independent loading scenarios applied in determination of the effective elastic properties are considered and the plotted stress and strain contours display the components corresponding to the nonzero macroscopic strain component in each case. For $E_2/E_1 = 10^{-4}$, due to high level of phase contrast, the applied macroscopic strain is mainly accommodated by the softer phase at which significant strain localization occurs. With the use of periodic boundary conditions, a significant waviness occurs in the volume element face. Once the phase contrast is decreased from $E_2/E_1 = 10^{-4}$ to $E_2/E_1 = 10^{-1}$, the periodic oscillations at the volume element face significantly dissipate and the deformed volume element shapes resemble those of the kinematic uniform loading case in which the volume
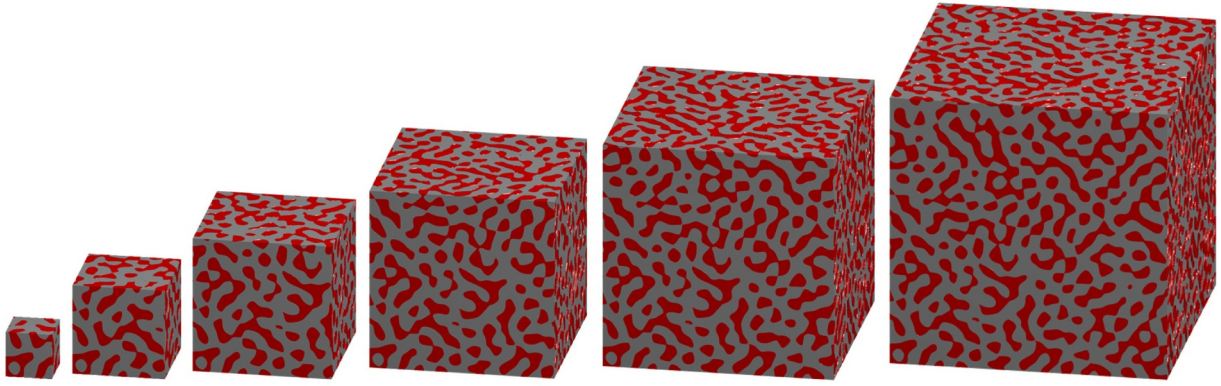
Fig. 4. Volume elements with side lengths of (left to right) 3, 6, 9, 12, 15 and 18 wavelengths. In these generations, phase 1 (red) / phase 2 (grey) volume fraction of $\phi_1 = 0.40$ is considered. In the corresponding finite element models, with constant voxel size for normalized RVE sizes, 0.6, 1.2, 1.8, 2.4, 3.0 and 3.6, $32 \times 32 \times 32$, $64 \times 64 \times 64$, $96 \times 96 \times 96$, $128 \times 128 \times 128$, $160 \times 160 \times 160$ and $192 \times 192 \times 192$ discretizations are used, respectively. (For interpretation of the references to colour in this figure legend, the reader is referred to the web version of this article.)

(a)   (b)
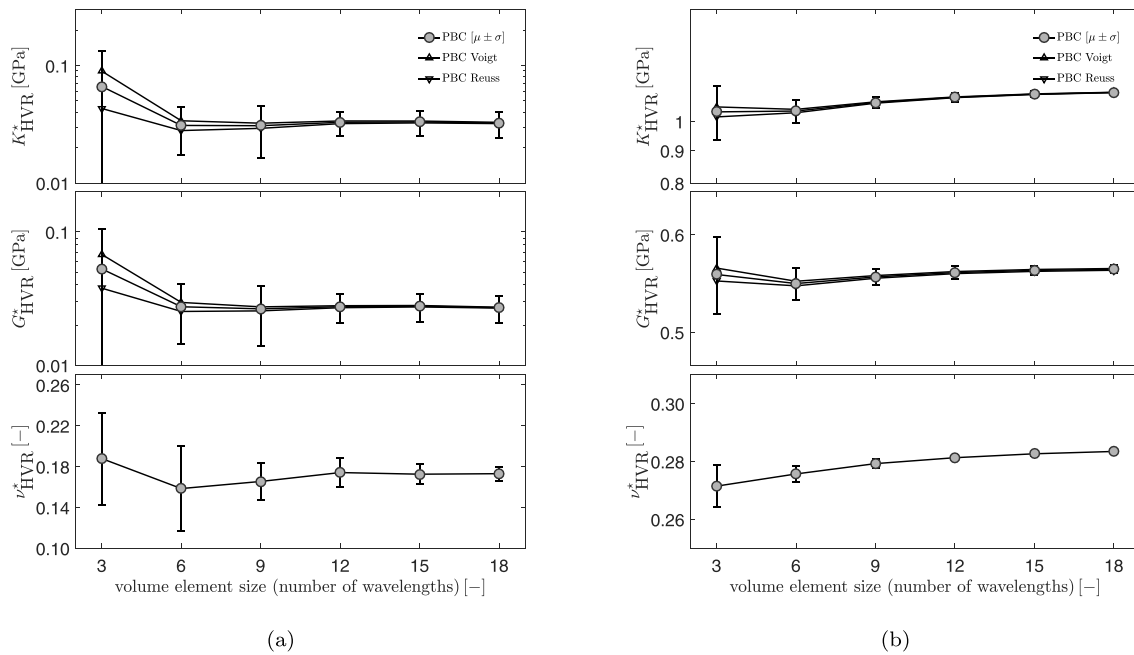
Fig. 5. Convergence of elastic properties with increasing volume element size for (a) $\phi_1 \simeq 0.20$ and (b) $\phi_1 \simeq 0.50$ and phase contrast of $E_2/E_1 = 0$ as input. The mean values converge to the desired effective values with corresponding error bars getting smaller as the volume element size increases. Periodic boundary conditions are used in the simulations. Based on the results, the minimum RVE size is selected to be 12 wavelengths. Detailed numerical values are listed in Tables B.1 and B.2. Data is presented as mean value μ (dots) and standard deviation σ from analysis of 5 random realizations. Lines merge mean values.

element faces remain flat. As compared to the results for $E_2/E_1 = 10^{-4}$, a relatively more balanced distribution of deformation between both phases is observed for $E_2/E_1 = 10^{-1}$. Similar comments apply for the demonstrated results in Figs. 8 and 9 where $\phi_1 \simeq 0.50$ is considered. This time, however, these localizations are less severe and the oscillations in the volume element face is reduced. Considering the stress development, with the improved force transmission along dense and continuous network of the stiff phase much larger stresses are observed for $\phi_1 \simeq 0.50$.

The results for intermediate phase contrast values are demonstrated in Fig. 10 and tabulated in Tables B.3 and B.4. Corresponding analytical bounds are listed in Tables B.5–B.8. In agreement with our observations on the strain and stress contours for different phase volume fraction ratios, for $\phi_1 \simeq 0.20$, there is a monotonically decreasing trend in the composite elastic stiffness with increasing phase contrast. This shows that the relative significance of the compliant phase in overall composite stiffness for $\phi_1 \simeq 0.20$ is higher than that for $\phi_1 \simeq 0.50$ in which

we observe a saturating composite macroscopic stiffness behavior towards $E_2/E_1 \to 0$. This signals a dominant contribution of the stiffer phase. At the other end, that is for $E_2/E_1 = 1$, single phase elastic properties are recovered. The observed Poisson's ratios decrease from 0.44 to 0.17 and to 0.28 approximately as phase contrast is changed from $E_2/E_1 = 1$ to $E_2/E_1 = 0$ for $\phi_1 \simeq 0.20$ and $\phi_1 \simeq 0.50$, respectively. Similar to the composite bulk and shear modulus, the Poisson's ratio for the latter case also saturates towards $E_2/E_1 \to 0$.

Plots for the Hashin-Shtrikman (HS) and the three-point Beran-Molyneux (BM) (for the bulk modulus) and the Milton-Phan-Tien (MPT) (for the shear modulus) bounds are also shown in Fig. 10. As required, none of the computational results violate the analytical bounds. As anticipated, the three-point Beran-Molyneux bounds (for the bulk modulus) and the Milton-Phan-Tien bounds (for the shear modulus) are much more stringent than the Hashin-Shtrikman bounds. To evaluate the three-point bounds we need to know the parameters η_i and ζ_i (see Eq. (A.2) in Appendix A), which depend on the underlying Gaussian
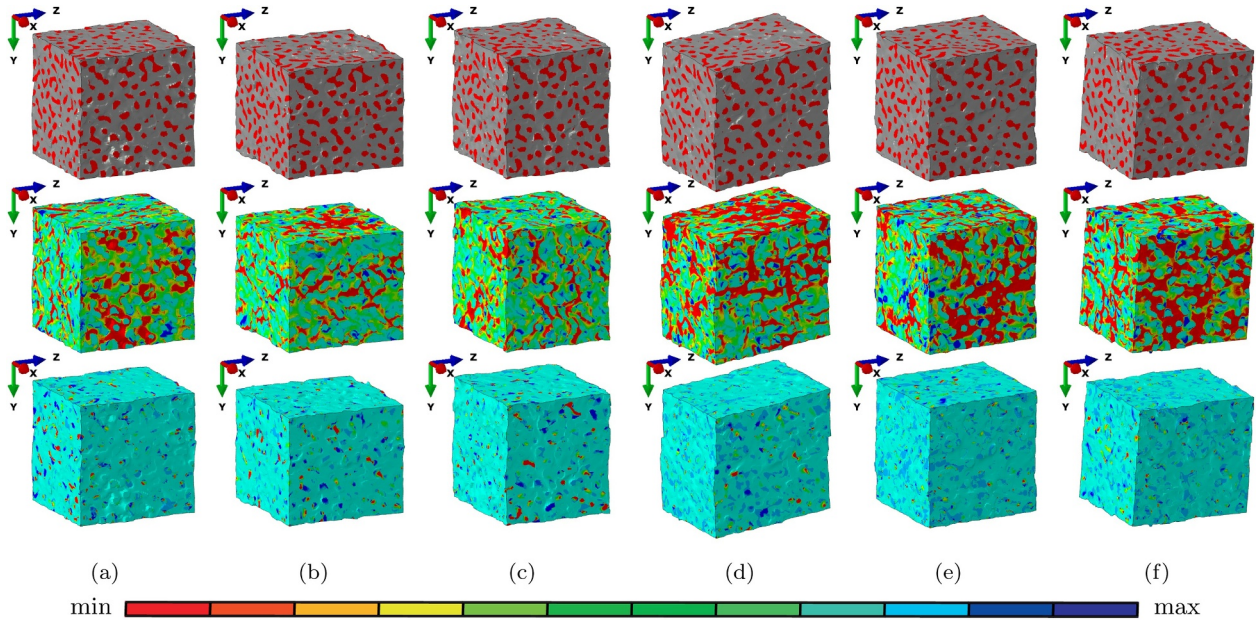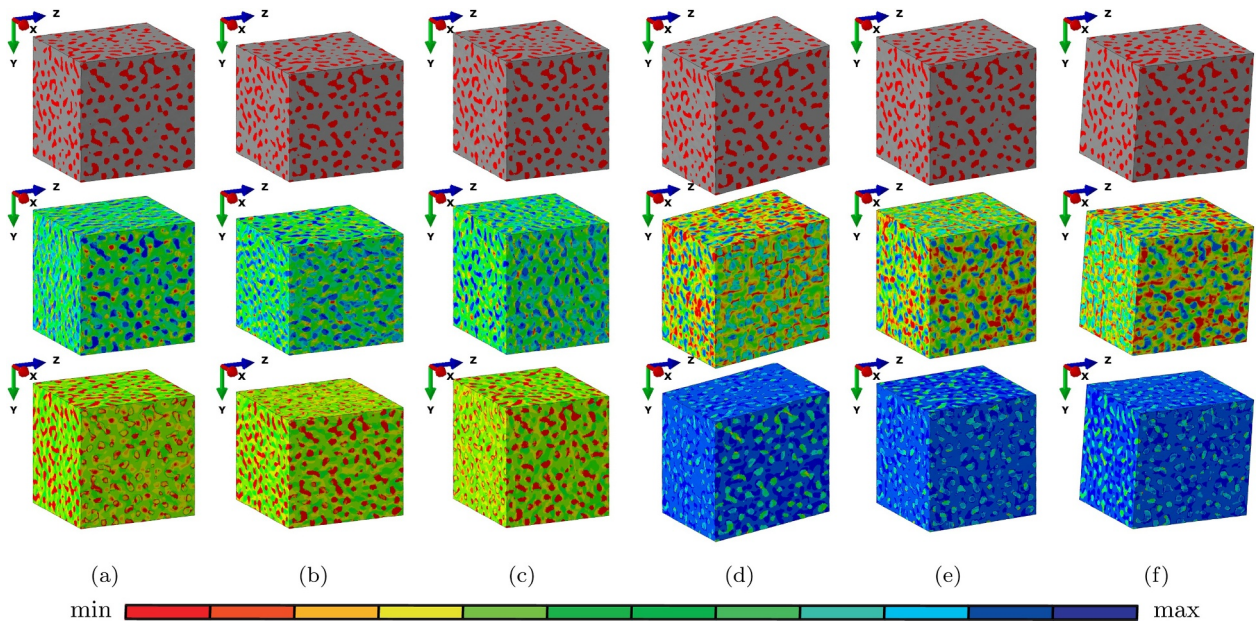
Fig. 6. Strain (row 2) and stress (row 3) plots over the volume elements for $\phi_1 \simeq 0.20$ and $E_2/E_1 = 10^{-4}$ for six independent loading cases: (a) $\varepsilon_{11}/\sigma_{11}$, (b) $\varepsilon_{22}/\sigma_{22}$, (c) $\varepsilon_{33}/\sigma_{33}$, (d) $\varepsilon_{23}/\sigma_{23}$, (e) $\varepsilon_{13}/\sigma_{13}$, (f) $\varepsilon_{12}/\sigma_{12}$. For strain resp. stress, legend max is 0.001 [−] resp. 2.5 [MPa] and legend min is − 0.0025 [−] resp. − 7.5 [MPa]. In top row, phase 1 resp. 2 is displayed in red resp. grey. A uniform deformation scaling of 100 is applied. The results are given for one of the stochastically realized microstructures. Periodic boundary conditions are applied. (For interpretation of the references to colour in this figure legend, the reader is referred to the web version of this article.)

random field used to generate the microstructure. The curves shown in Fig. 10 were obtained by using the values that were tabulated in Roberts and Teubner (1995) and Roberts and Garboczi (2002) corresponding to different Gaussian random fields. Both curves are almost indistinguishable, hence indicating that the analytical three-points bounds are insensitive to the fine details of the underlying random field, something that was already mentioned in Roberts and Knackstedt (1996). Therefore, even though the random function used in our work, Eq. (2), to generate the microstructures has slightly different statistics to the functions used in Refs. Roberts and Teubner (1995) and

Roberts and Garboczi (2002) (see Appendix A for more details), the three-point bounds shown in Fig. 10 are valid for the microstructures studied in this work.

As Fig. 10 shows, for the material contrast range of $E_2/E_1 < 10^{-1}$, analytical bounds give a sufficiently narrow prediction. For $E_2/E_1 > 10^{-4}$ and for $\phi_1 \simeq 0.20$ the computed effective bulk and shear moduli tend to be closer to the lower bounds whereas for the same region for $\phi_1 \simeq 0.50$ computations tend to be closer to the upper bounds. Nevertheless, in general, for the selected cases the effective composite properties cannot be accurately predicted by the analytical

Fig. 7. Strain (row 2) and stress (row 3) plots over the volume elements for $\phi_1 \simeq 0.20$ and $E_2/E_1 = 10^{-1}$ for six independent loading cases: (a) $\varepsilon_{11}/\sigma_{11}$, (b) $\varepsilon_{22}/\sigma_{22}$, (c) $\varepsilon_{33}/\sigma_{33}$, (d) $\varepsilon_{23}/\sigma_{23}$, (e) $\varepsilon_{13}/\sigma_{13}$, (f) $\varepsilon_{12}/\sigma_{12}$. For strain resp. stress, legend max is 0 resp. 0 and legend min is − 0.0025 [−] resp. − 50 [MPa]. In top row, phase 1 resp. 2 is displayed in red resp. grey. A uniform deformation scaling of 100 is applied. The results are given for one of the stochastically realized microstructures. Periodic boundary conditions are applied. (For interpretation of the references to colour in this figure legend, the reader is referred to the web version of this article.)
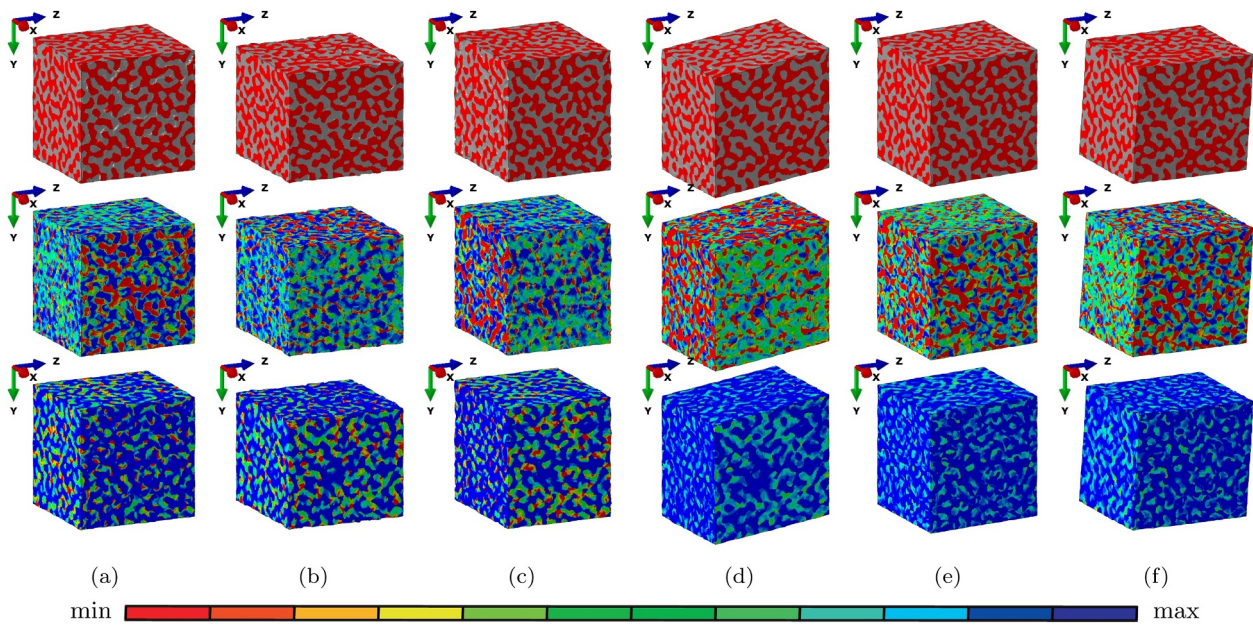
Fig. 8. Strain (row 2) and stress (row 3) plots over the volume elements for $\phi_1 \simeq 0.50$ and $E_2/E_1 = 10^{-4}$ for six independent loading cases: (a) $\varepsilon_{11}/\sigma_{11}$, (b) $\varepsilon_{22}/\sigma_{22}$, (c) $\varepsilon_{33}/\sigma_{33}$, (d) $\varepsilon_{23}/\sigma_{23}$, (e) $\varepsilon_{13}/\sigma_{13}$, (f) $\varepsilon_{12}/\sigma_{12}$. For strain resp. stress, legend max is 0.001 [−] resp. 0 and legend min is − 0.0025 [−] resp. − 100 [MPa]. In top row, phase 1 resp. 2 is displayed in red resp. grey. A uniform deformation scaling of 100 is applied. The results are given for one of the stochastically realized microstructures. Periodic boundary conditions are applied. (For interpretation of the references to colour in this figure legend, the reader is referred to the web version of this article.)
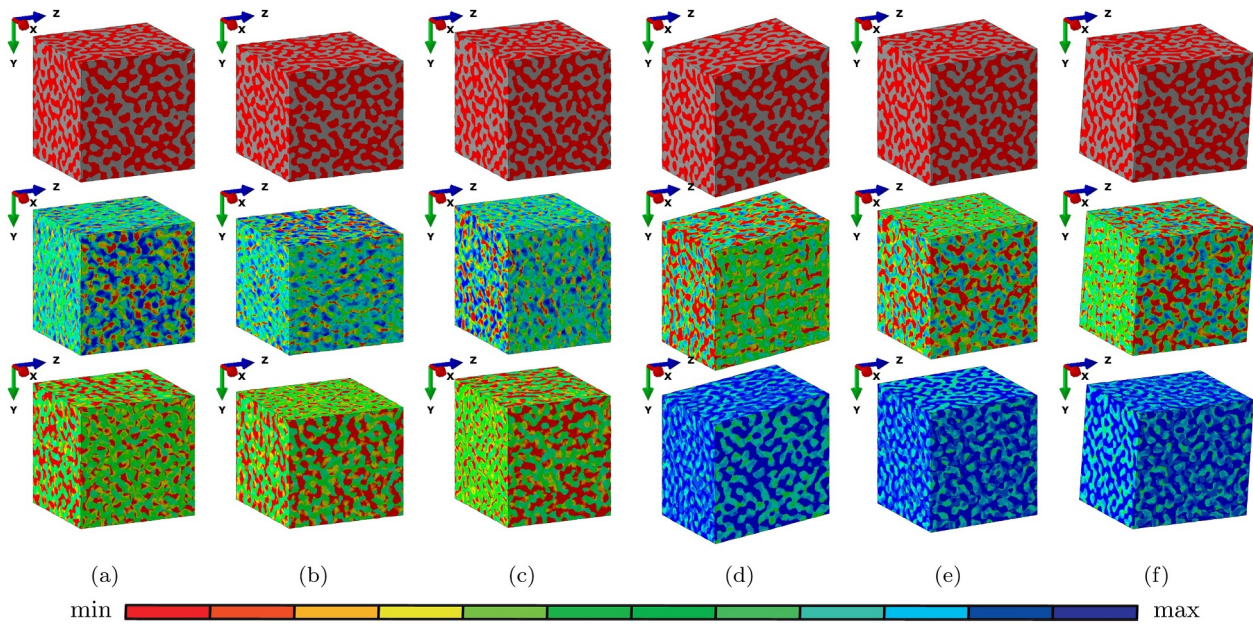
Fig. 9. Strain (row 2) and stress (row 3) plots over the volume elements for $\phi_1 \simeq 0.50$ and $E_2/E_1 = 10^{-1}$ for six independent loading cases: (a) $\varepsilon_{11}/\sigma_{11}$, (b) $\varepsilon_{22}/\sigma_{22}$, (c) $\varepsilon_{33}/\sigma_{33}$, (d) $\varepsilon_{23}/\sigma_{23}$, (e) $\varepsilon_{13}/\sigma_{13}$, (f) $\varepsilon_{12}/\sigma_{12}$. For strain/stress, legend max is 0 resp. 0 and legend min is − 0.0025 [−] resp. − 100 [MPa]. In top row, phase 1 resp. 2 is displayed in red/grey. A uniform deformation scaling of 100 is applied. The results are given for one of the stochastically realized microstructures. Periodic boundary conditions are applied. (For interpretation of the references to colour in this figure legend, the reader is referred to the web version of this article.)

bounds. This is the case especially for lower metal volume fractions.

3.3. Effective elastic properties of metal-polymer nanocomposites and associated scaling law

In the final part of this section, we investigate the effective elastic properties of metal-polymer nanocomposites. To this end, (stiff) phase 1 and (compliant) phase 2 are selected as gold and epoxy resin, respectively, where the latter has a Young's modulus of 1.038 GPa and a Poisson's ratio of 0.35 (Bargmann et al., 2016; Wang and Weissmüller,

2013).

Effective properties of the gold-polymer nanocomposites are computed for volume elements of 12 wavelength size (see Section 3.1) and under periodic boundary conditions. Results of the Young's moduli and the Poisson's ratios for various phase volume distributions are demonstrated in Fig. 11 and tabulated in Table B.9. A linear trend in log-log scale is evident for the plotted Young's moduli values with respect to the gold phase's volume fraction. This trend is quite different from what is observed in nanoporous gold. Although in nanoporous gold, the load is transmitted along gold ligaments which hinges upon the phase
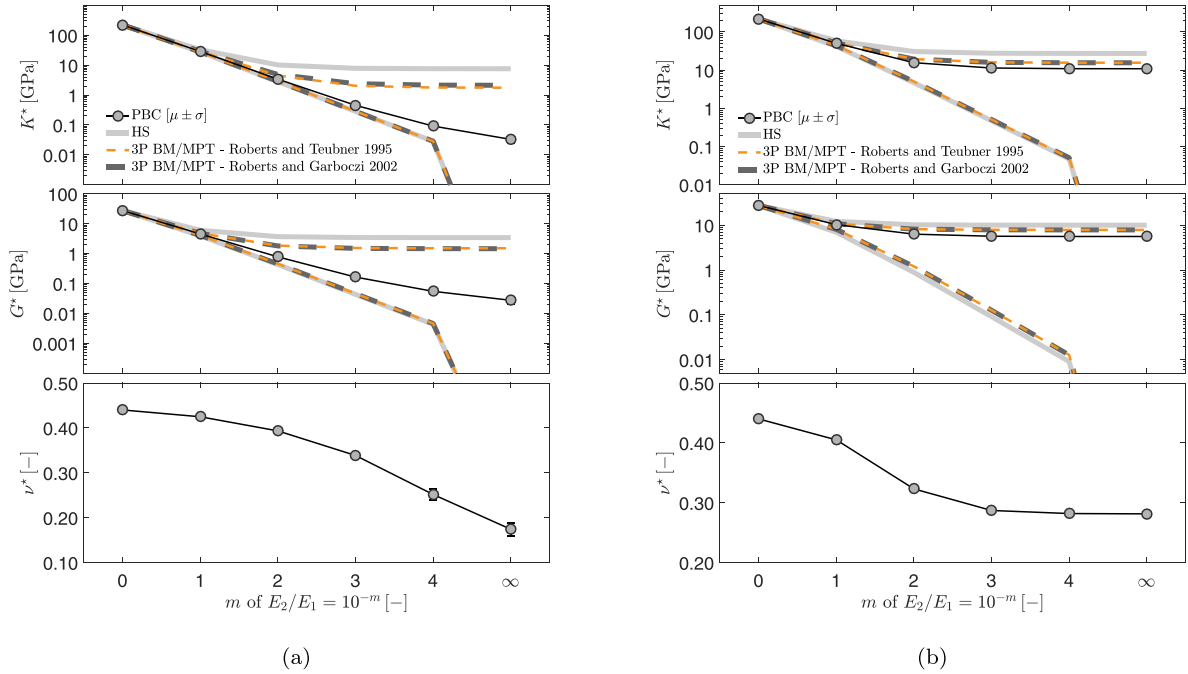
Fig. 10. Influence of phase contrast on the computed effective elastic properties for (a) $\phi_1 \simeq 0.20$ and (b) $\phi_1 \simeq 0.50$. Detailed numerical values of the computations are listed in Tables B.3 and B.4 and of the bounds are listed in Tables B.6–B.8. Periodic boundary conditions are used in the simulations. Plots for the Hashin-Shtrikman (HS) and the three-point Beran-Molyneux (BM) (for the bulk modulus) and the Milton-Phan-Tien (MPT) (for the shear modulus) bounds are also shown. As required, none of the computational results violate the analytical bounds. As anticipated, the three-point Beran-Molyneux bounds (for the bulk modulus) and the Milton-Phan-Tien bounds (for the shear modulus) are much stringent then the Hashin-Shtrikman bounds. The two curves given for each of the three-point bounds are created with the tabulated η_i and ζ_i values (see Eq. (A.2)) corresponding to the Gaussian random fields studied in Roberts and Teubner (1995) and Roberts and Garboczi (2002). Data is presented as mean value μ (dots) and standard deviation σ from analysis of 5 random realizations. Lines merge mean values.
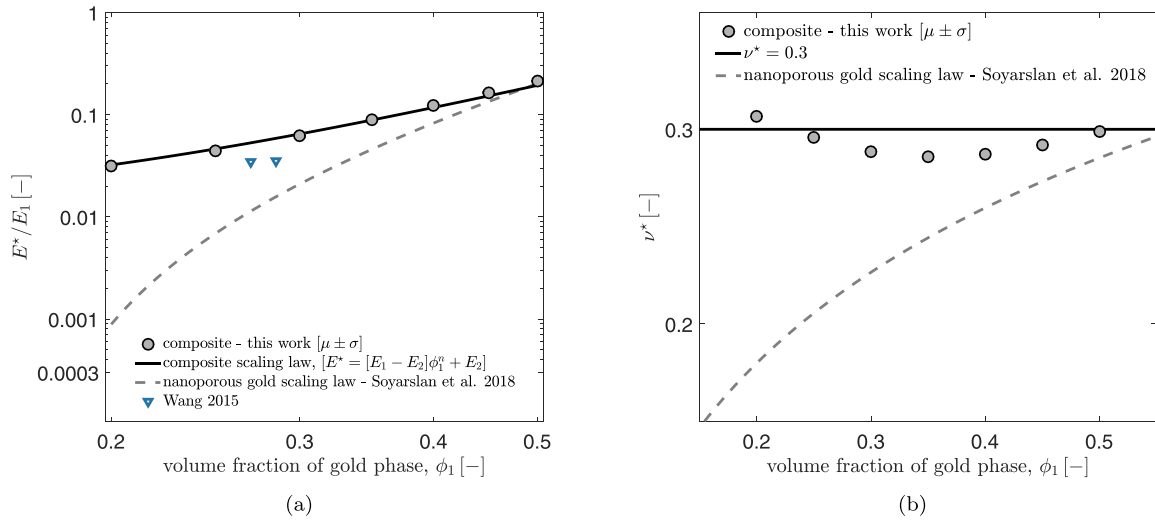
Fig. 11. (a) Scaling law for the Young's modulus for gold-epoxy composite as a function of the gold phase (denoted as phase 1) volume fraction. Considering that epoxy is considerably compliant as compared to gold the results for the composite Young's modulus are reported as a factor of the Young's modulus gold. The scaling law with $n \simeq 2.45$ for bicontinuous gold-polymer composites generated by the leveled-wave model provides higher elastic modulus then a very limited number of experimentally obtained effective elasticity moduli reported in Wang (2015) for gold volume fractions around $0.27 - 0.285$. (b) For the selected volume fraction range, the Poisson's ratio of the composite varies around 0.3. Data is presented as mean value μ (dots) and standard deviation σ from analysis of 5 random realizations.

topology through network connectivity, in the space filling composite, force transmission is ensued in all directions without cease. Thus, in metal-polymer composites, loss of metal percolation does not result in structural collapse, as it does in nanoporous metals. For the current gold-epoxy composite, the lost stiffness with greatly reduced connectivity among load bearing ligaments is compensated by that of impregnated epoxy despite of the relatively high phase contrast with

$E_2/E_1 = E_{epoxy}/E_{gold} \simeq 0.0131$. The consequent linear behavior at this scale well agrees with the composite scaling law proposed in Carolan et al. (2015) as a simple adaptation of the Gibson and Ashby law (Gibson and Ashby, 1997) which is largely used for cellular materials with invariant topological properties under relative density changes

$$E^\star = [E_1 - E_2]\phi_1^n + E_2. \tag{42}$$

Here, E_2 represents the Young's modulus of the compliant phase, which, in the current case is epoxy resin. $n \simeq 2.45$ is used in the depicted plot of the scaling law in Fig. 11. With this scaling law $E^\star = E_1$ is recovered at $\phi_1 = 1$ and $E^\star = E_2$ at $\phi_1 = 0$. These computations result in a stiffer response as compared to a very limited number of experimental results with composite elasticity moduli of $E^\star = 2.78$ and $E^\star = 2.74$ GPa for ligament diameters of 20 and 50 nm and gold volume fraction around $0.27 - 0.285$ with epoxy elasticity modulus of $E_2 = 1.05$ GPa (Wang, 2015). For $E_2 \to 0$ Gibson and Ashby scaling law (Gibson and Ashby, 1997) for open-cell foams is recovered which is shown to be inaccurate for nanoporous gold Soyarslan et al. (2018b). Accuracy of the scaling law given in Eq. (42) is expected to deteriorate for composites with phase contrasts higher than that of gold-polymer composites such that at $E_2 = 0$, nanoporous gold scaling law given in Fig. 11 should be satisfied.

As opposed to the monotonic and relatively sharp decrease of the Poisson's ratio with reducing gold phase volume fraction ϕ_1 in nanoporous gold, the Poisson's ratio of the metal-polymer composite exhibits a nonmonotonic trend with a minimum of $\nu^\star \simeq 0.286$ at $\phi_1 \simeq 0.35$ for the observed gold phase volume fraction interval. Considering that the bulk Poisson's ratio's of both gold and epoxy are larger than 0.3, this is attributed to the mutual structural effects dominated by the stiffer gold phase network rather than local bulk deformation effects of the phases which considerably reduces the composite's effective Poisson's ratio.

4. Conclusions

In this work, based on a finite element-based asymptotic homogenization scheme and an efficient and robust method for generating 3D random and heterogeneous bicontinuous microstructures, the influence of the volume element size, phase contrast, relative volume fraction of phases and applied boundary conditions on the estimated macroscopic elastic properties is investigated. Using the determined RVE size we computed the effective elastic properties of gold-epoxy nanocomposites of various phase volume fractions which agree well with the recorded literature. These results are also in agreement with the composite scaling law proposed in Carolan et al. (2015) as an adaptation of the Gibson and Ashby law (Gibson and Ashby, 1997) which is largely used for cellular materials with invariant topological properties under relative density changes.

The major outcomes of this work are:

- In bicontinuous metal-polymer composites, compliant phase impregnation compensates for the stiffness loss due to topological changes in the stiffer phase with corresponding volume fraction reduction towards stiffer phase percolation threshold. This results in a distinct scaling relation for the elastic stiffness of the composite.
- Considering a large interval of relative phase volume fractions and high phase contrast only periodic boundary conditions provide effective elastic moduli at reasonably small volume element sizes. At this size, only for bicontinuous composites with a phase contrast of $E_2/E_1 > 10^{-1}$, the boundary condition influence on the computed apparent properties can be disregarded.[4]
- Even the third-order analytical bounds are not stringent enough to serve determination of effective elastic properties of bicontinuous metal-polymer composites. Thus, computational homogenization devising periodic boundary conditions is an indispensable tool in efficient and accurate determination of the effective properties of 3D bicontinuous random composites with high contrast and volume fraction bias towards the weaker phase.

Appendix A. Analytical bounds for bicontinuous random composites

In this part, we summarize rigorous bounds on effective bulk and shear moduli of random materials. These bounds devise certain microstructural informations, e.g., phase volume fraction and $n-$point correlations functions. Defining the indicator function $\Theta(\boldsymbol{x}) = 1$ if $\boldsymbol{x} \in \mathcal{B}_1$ and 0 otherwise, we define the following quantities

$$
\begin{aligned}
\phi_1 &= \langle \Theta(\boldsymbol{x}) \rangle, \\
S_2(r) &= \langle \Theta(\boldsymbol{x}_i)\Theta(\boldsymbol{x}_j) \rangle, \\
S_3(r, s, t) &= \langle \Theta(\boldsymbol{x}_i)\Theta(\boldsymbol{x}_j)\Theta(\boldsymbol{x}_k) \rangle,
\end{aligned}
\tag{A.1}
$$

where S_2 and S_3 are the two- and three-point correlation function. Since the random field is statistically stationary and isotropic, these correlation functions only depend on the distances $r = |\boldsymbol{x}_i - \boldsymbol{x}_j|$, $s = |\boldsymbol{x}_j - \boldsymbol{x}_k|$, and $t = |\boldsymbol{x}_i - \boldsymbol{x}_k|$ (Roberts and Garboczi, 2002).

To evaluate the three-point bounds, parameters η_i and ζ_i for $i = 1, 2$ have to be computed using (Torquato, 1991; Roberts and Knackstedt, 1996; Roberts and Garboczi, 2002)

$$
\zeta_i = \frac{9}{2\phi_1\phi_2} \int_0^\infty \frac{dr}{r} \int_0^\infty \frac{ds}{s} \int_{-1}^1 P_2(\cos\theta)\left[S_3^{(i)}(r, s, t) - \frac{S_2^{(i)}(r)S_2^{(i)}(s)}{\phi_1} \right] d(\cos\theta),
$$

$$
\eta_i = \frac{5\zeta_i}{21} + \frac{150}{7\phi_1\phi_2} \int_0^\infty \frac{dr}{r} \int_0^\infty \frac{ds}{s} \int_{-1}^1 P_4(\cos\theta)\left[S_3^{(i)}(r, s, t) - \frac{S_2^{(i)}(r)S_2^{(i)}(s)}{\phi_1} \right] d(\cos\theta).
\tag{A.2}
$$

Here, P_2 and P_4 denote second- and fourth-order Legendre polynomials, respectively. For a randomly inserted triangle in the sample, $S_3^{(i)}(r, s, t)$ is the probability of finding phase i in the vertices of the triangle with edge lengths of r, s and t. For two-phase composites, $\phi_1 + \phi_2 = 1$, $\zeta_1 + \zeta_2 = 1$ and $\eta_1 + \eta_2 = 1$. Tabulated values of these parameters have been reported in Roberts and Teubner (1995) and Roberts and Garboczi (2002) for different Gaussian random fields, which are characterized by different field-field correlation functions. The field-field correlation function of the Gaussian random function used in our work is $C(r) = \sin(q_0 r)/q_0 r$ (see Soyarslan et al. (2018b) for details), which is different to that of any of the models used in Roberts and Teubner (1995) and Roberts and Garboczi (2002). However, as was discussed in Roberts and Knackstedt (1996), parameters ζ_i and η_i are found to be relatively insensitive to the fine details of the microstructure statistical properties. Therefore, to compute the analytical three-point

---

[4] Currently studied gold-epoxy composite have higher phase contrasts with $E_2/E_1 < 10^{-1}$. Bicontinuous composites of rubber-photopolymer (Al-Ketan et al., 2017), bicontinuous binary polymers (Carolan et al., 2015) and composites of polymer-elastomer (Wang et al., 2011) exhibit relatively smaller phase contrast.

bounds we directly use the numerical values tabulated in Roberts and Teubner (1995) and Roberts and Garboczi (2002)—we also note that an additional justification for doing so is that for sufficiently small distances, all field-field correlation functions have in fact the same expression $C(r) \sim 1 - ar^2$, where a is a constant (Roberts and Knackstedt, 1996).

Weighted arithmetic and harmonic averages of the constituent elastic moduli, which are referred to as Voigt and Reuss bounds constitute the earliest rigorous bounds on the effective material properties of two-phase materials (Hill, 1952). A slightly more involved bound which is valid for well-ordered random materials[5], that is $[K_2 - K_1][G_2 - G_1] \geq 0$, is the Hashin–Shtrikman bound (Hashin and Shtrikman, 1963). Using the notation

$$\langle\{\bullet\}\rangle_\phi = \phi_1\{\bullet\}_1 + \phi_2\{\bullet\}_2 \quad \text{and} \quad \langle\{\tilde{\bullet}\}\rangle_\phi = \phi_2\{\bullet\}_1 + \phi_1\{\bullet\}_2,$$
$$\langle\{\bullet\}\rangle_\eta = \eta_1\{\bullet\}_1 + \eta_2\{\bullet\}_2 \quad \text{and} \quad \langle\{\bullet\}\rangle_\zeta = \zeta_1\{\bullet\}_1 + \zeta_2\{\bullet\}_2, \tag{A.3}$$

and for $K_1 < K_2$ and $G_1 < G_2$, it reads for $K^\star$ and $G^\star$

$$K_{\text{L,HS}} \leq K^\star \leq K_{\text{U,HS}} \quad \text{and} \quad G_{\text{L,HS}} \leq G^\star \leq G_{\text{U,HS}}, \tag{A.4}$$

where

$$K_{\text{L,HS}} = K_1 + \frac{\phi_2}{[K_2 - K_1]^{-1} + 3\phi_1[3K_1 + 4G_1]^{-1}},$$
$$K_{\text{U,HS}} = K_2 + \frac{\phi_1}{[K_1 - K_2]^{-1} + 3\phi_2[3K_2 + 4G_2]^{-1}}, \tag{A.5}$$

and

$$G_{\text{L,HS}} = G_1 + \frac{\phi_2}{[G_2 - G_1]^{-1} + 6\phi_1[K_1 + 2G_1][5G_1[3K_1 + 4G_1]]^{-1}},$$
$$G_{\text{U,HS}} = G_2 + \frac{\phi_1}{[G_1 - G_2]^{-1} + 6\phi_2[K_2 + 2G_2][5G_2[3K_2 + 4G_2]]^{-1}}. \tag{A.6}$$

The simplified form of the three-point Beran and Molyneux (1966) bounds by Milton (1981) for the effective bulk modulus $K^\star$ reads

$$K_{\text{L,BM}} \leq K^\star \leq K_{\text{U,BM}}, \tag{A.7}$$

where

$$K_{\text{L,BM}} = \left[\langle K^{-1}\rangle_\phi - \frac{4\phi_1\phi_2[K_2^{-1} - K_1^{-1}]^2}{4\langle\tilde{K}^{-1}\rangle_\phi + 3\langle G^{-1}\rangle_\zeta}\right]^{-1},$$
$$K_{\text{U,BM}} = \langle K\rangle_\phi - \frac{3\phi_1\phi_2[K_2 - K_1]^2}{3\langle\tilde{K}\rangle_\phi + 4\langle G\rangle_\zeta}. \tag{A.8}$$

Finally, the Milton-Phan-Thien three-point bounds (Milton and Phan-Thien, 1982) for $G^\star$ read

$$G_{\text{L,MPT}} \leq G^\star \leq G_{\text{U,MPT}}, \tag{A.9}$$

where

$$G_{\text{L,MPT}} = \left[\langle G^{-1}\rangle_\phi - \frac{\phi_1\phi_2[G_2^{-1} - G_1^{-1}]^2}{\langle\tilde{G}^{-1}\rangle_\phi + 6\Omega_{\text{MPT}}}\right]^{-1},$$
$$G_{\text{U,MPT}} = \langle G\rangle_\phi - \frac{6\phi_1\phi_2[G_2 - G_1]^2}{6\langle\tilde{G}\rangle_\phi + \Lambda_{\text{MPT}}}, \tag{A.10}$$

with

$$\Omega_{\text{MPT}} = \frac{5\langle G^{-1}\rangle_\zeta\langle 6K^{-1} - G^{-1}\rangle_\zeta + \langle G^{-1}\rangle_\eta\langle 2K^{-1} + 21G^{-1}\rangle_\zeta}{\langle 128K^{-1} + 99G^{-1}\rangle_\zeta + 45\langle G^{-1}\rangle_\eta},$$
$$\Lambda_{\text{MPT}} = \frac{3\langle G\rangle_\eta\langle 6K + 7G\rangle_\zeta - 5\langle G\rangle_\zeta^2}{\langle 2K - G\rangle_\zeta + 5\langle G\rangle_\eta}. \tag{A.11}$$

For further bounds and details on derivations, the reader is referred to the original articles and works of Quintanilla (1999) and Torquato (1991).

Appendix B. Detailed numerical results

In this part, we tabulate some numerical results corresponding to the depicted plots.

---

[5] A generalization of the Hashin–Shtrikman bounds to badly-ordered materials can be found in Walpole (1969).

Table B1

Computed apparent elastic properties for various volume element sizes for $\phi_1 \simeq 0.20$ phase volume fraction. λ corresponds to the wavelength. Here, $E_2/E_1 = 0$ with $E_1 = 79$ GPa and $\nu_1 = 0.44$ which gives $K_1 \simeq 219444.44$ MPa and $G_1 \simeq 27430.56$ MPa.

volume element size [λ]	Periodic BC							Kinematically Uniform BC						
	$K^\star_{HVR}$ [MPa]	$G^\star_{HVR}$ [MPa]	$\nu^\star_{HVR}$ [−]	Err $K^\star$ [−]	Err $G^\star$ [−]	Err $\nu^\star$ [−]	$A^\star_U$ [−]	$K^\star_{HVR}$ [MPa]	$G^\star_{HVR}$ [MPa]	$\nu^\star_{HVR}$ [−]	Err $K^\star$ [−]	Err $G^\star$ [−]	Err $\nu^\star$ [−]	$A^\star_U$ [−]
3	66.37 ± 65.64	52.77 ± 51.55	0.1878 ± 0.0450	1.1449	0.9218	0.1854	≫1	1783.59 ± 345.74	1190.96 ± 217.52	0.2265 ± 0.0060	1.1689	1.0693	0.0468	2.69×10^{-1}
6	30.94 ± 13.51	27.46 ± 13.08	0.1584 ± 0.0419	0.0052	0.0364	0.0421	1.26×10^{0}	822.36 ± 89.08	575.52 ± 64.86	0.2163 ± 0.0048	0.5133	0.5054	0.0055	1.39×10^{-1}
9	30.78 ± 14.52	26.50 ± 12.64	0.1654 ± 0.0180	0.0650	0.0363	0.0500	5.71×10^{-1}	543.42 ± 53.56	382.30 ± 39.23	0.2151 ± 0.0024	0.3376	0.3275	0.0086	1.34×10^{-1}
12	32.92 ± 7.72	27.49 ± 6.88	0.1741 ± 0.0144	0.0062	0.0083	0.0093	2.27×10^{-1}	406.26 ± 29.68	287.99 ± 21.34	0.2133 ± 0.0021	0.2438	0.2399	0.0033	1.41×10^{-1}
15	33.13 ± 7.86	27.72 ± 6.47	0.1725 ± 0.0099	0.0199	0.0251	0.0029	1.62×10^{-1}	326.63 ± 20.50	232.27 ± 15.21	0.2126 ± 0.0027	0.1978	0.1926	0.0046	1.48×10^{-1}
18	32.48 ± 8.16	27.04 ± 6.22	0.1730 ± 0.0070	–	–	–	1.06×10^{-1}	272.69 ± 19.02	194.75 ± 14.25	0.2116 ± 0.0019	–	–	–	1.51×10^{-1}

13

Table B2

Computed apparent elastic properties for various volume element sizes for $\phi_1 \simeq 0.50$ phase volume fraction. λ corresponds to the wavelength. Here, $E_2/E_1 = 0$ with $E_1 = 79$ GPa and $\nu_1 = 0.44$ which gives $K_1 \simeq 219444.44$ MPa and $G_1 \simeq 27430.56$ MPa.

Periodic BC

volume element size [λ]	$K^\star_{HVR}$ [MPa]	$G^\star_{HVR}$ [MPa]	$\nu^\star_{HVR}$ [−]	Err $K^\star$ [−]	Err $G^\star$ [−]	Err $\nu^\star$ [−]	$A^\star_U$ [−]
3	10353.70 ± 1015.87	5569.03 ± 399.16	0.2715 ± 0.0072	0.0030	0.0171	0.0153	1.59× 10^{-1}
6	10384.90 ± 439.12	5475.59 ± 165.68	0.2757 ± 0.0027	0.0304	0.0123	0.0128	5.60× 10^{-2}
9	10710.68 ± 218.84	5543.92 ± 79.00	0.2793 ± 0.0015	0.0187	0.0080	0.0072	3.00× 10^{-2}
12	10915.24 ± 176.32	5588.84 ± 66.48	0.2813 ± 0.0009	0.0112	0.0041	0.0048	2.21× 10^{-2}
15	11039.29 ± 129.91	5611.59 ± 50.45	0.2827 ± 0.0007	0.0062	0.0019	0.0028	2.01× 10^{-2}
18	11108.62 ± 110.39	5622.38 ± 42.92	0.2835 ± 0.0005	[−]	[−]	[−]	1.76× 10^{-2}

Kinematically Uniform BC

volume element size [λ]	$K^\star_{HVR}$ [MPa]	$G^\star_{HVR}$ [MPa]	$\nu^\star_{HVR}$ [−]	Err $K^\star$ [−]	Err $G^\star$ [−]	Err $\nu^\star$ [−]	$A^\star_U$ [−]
3	16967.95 ± 1292.59	8039.73 ± 386.82	0.2951 ± 0.0051	0.2180	0.1674	0.0255	6.71× 10^{-2}
6	13930.76 ± 468.13	6886.96 ± 149.09	0.2877 ± 0.0022	0.0587	0.0553	0.0019	3.46× 10^{-2}
9	13158.40 ± 220.41	6525.88 ± 67.39	0.2872 ± 0.0013	0.0322	0.0313	0.0005	2.26× 10^{-2}
12	12747.86 ± 182.22	6327.61 ± 60.19	0.2870 ± 0.0009	0.0180	0.0188	0.0006	1.73× 10^{-2}
15	12522.87 ± 120.82	6210.63 ± 43.32	0.2872 ± 0.0006	0.0136	0.0141	0.0003	1.63× 10^{-2}
18	12354.86 ± 110.65	6124.06 ± 41.45	0.2873 ± 0.0005	—	-	-	1.44× 10^{-2}

Table B3

Computed apparent (KUBC) and effective (PBC) elastic properties for various phase contrast values for $\phi_1 \simeq 0.20$ phase volume fraction at RVE size determined using periodic boundary conditions. $E_1 = 79$ GPa and $\nu_1 = 0.44$ which gives $K_1 \simeq 219444.44$ MPa and $G_1 \simeq 27430.56$ MPa.

$\frac{E_2}{E_1}$ [−]	Periodic BC				Kinematically Uniform BC			
	$K^\star$ [MPa]	$G^\star$ [MPa]	$\nu^\star$ [−]	$A_U^\star$ [−]	$K^\star$ [MPa]	$G^\star$ [MPa]	$\nu^\star$ [−]	$A_U^\star$ [−]
0	32.92 ± 7.72	27.49 ± 6.88	0.1741 ± 0.0145	2.27×10^{-1}	406.26 ± 29.68	287.99 ± 21.34	0.2133 ± 0.0021	1.41×10^{-1}
10^{-4}	91.76 ± 11.47	54.89 ± 9.48	0.2517 ± 0.0115	8.32×10^{-2}	462.99 ± 32.20	313.05 ± 22.64	0.2241 ± 0.0028	1.04×10^{-1}
10^{-3}	452.91 ± 18.97	164.08 ± 12.99	0.3386 ± 0.0056	3.34×10^{-2}	818.98 ± 34.98	418.16 ± 23.37	0.2819 ± 0.0030	3.91×10^{-2}
10^{-2}	3388.35 ± 41.44	778.47 ± 22.43	0.3933 ± 0.0016	1.06×10^{-2}	3743.22 ± 51.18	1024.62 ± 29.19	0.3746 ± 0.0017	4.94×10^{-3}
10^{-1}	28623.75 ± 134.29	4530.55 ± 39.13	0.4248 ± 0.0003	5.32×10^{-4}	28888.93 ± 138.69	4709.93 ± 41.95	0.4227 ± 0.0003	5.05×10^{-4}
1	219444.44	27430.56	0.44	0	219444.44	27430.56	0.44	0

Table B4

Computed apparent (KUBC) and effective (PBC) elastic properties for various phase contrast values for $\phi_1 \simeq 0.50$ phase volume fraction at RVE size determined using periodic boundary conditions. $E_1 = 79$ GPa and $\nu_1 = 0.44$ which gives $K_1 \simeq 219444.44$ MPa and $G_1 \simeq 27430.56$ MPa.

$\frac{E_2}{E_1}$ [−]	Periodic BC				Kinematically Uniform BC			
	$K^\star$ [MPa]	$G^\star$ [MPa]	$\nu^\star$ [−]	$A_U^\star$ [−]	$K^\star$ [MPa]	$G^\star$ [MPa]	$\nu^\star$ [−]	$A_U^\star$ [−]
0	10915.24 ± 176.32	5588.85 ± 66.48	0.2813 ± 0.0009	2.21×10^{-2}	12747.86 ± 182.21	6327.61 ± 60.19	0.2870 ± 0.0009	1.73×10^{-2}
10^{-4}	10948.63 ± 98.51	5589.54 ± 34.10	0.2819 ± 0.0006	1.78×10^{-2}	12770.22 ± 92.37	6326.52 ± 28.89	0.2874 ± 0.0005	1.30×10^{-2}
10^{-3}	11402.06 ± 96.39	5661.32 ± 33.54	0.2870 ± 0.0006	1.70×10^{-2}	13200.14 ± 91.37	6387.85 ± 28.59	0.2916 ± 0.0005	1.26×10^{-2}
10^{-2}	15698.32 ± 83.63	6298.12 ± 29.26	0.3231 ± 0.0002	1.18×10^{-2}	17322.24 ± 83.94	6945.51 ± 25.98	0.3232 ± 0.0002	9.36×10^{-3}
10^{-1}	50568.34 ± 63.56	10257.59 ± 15.99	0.4050 ± 0.0000	1.59×10^{-3}	51538.27 ± 66.80	10620.36 ± 15.32	0.4036 ± 0.0000	1.54×10^{-3}
1	219444.44	27430.56	0.44	0	219444.44	27430.56	0.44	0

Table B5

Analytical Hashin-Shtrikman and the three-point Beran-Molyneux bounds for the bulk modulus for phase contrast values for $\phi_1 \simeq 0.20$ phase volume fraction. The two columns identified by I and II given for the three-point bounds are created with the tabulated η_i and ζ_i values (see Eq. A.2) corresponding to the Gaussian random fields studied in the Refs. Roberts and Teubner (1995) and Roberts and Garboczi (2002), respectively. $E_1 = 79$ GPa and $\nu_1 = 0.44$ which gives $K_1 \simeq 219444.44$ MPa and $G_1 \simeq 27430.56$ MPa.

$\frac{E_2}{E_1}$ [−]	Lower bounds			Upper bounds		
	$K_{L,HS}$ [MPa]	$K_{L,BM,I}$ [MPa]	$K_{L,BM,II}$ [MPa]	$K_{U,HS}$ [MPa]	$K_{U,BM,I}$ [MPa]	$K_{U,BM,II}$ [MPa]
0	0.00	0.00	0.00	7567.05	2116.47	1754.38
10^{-4}	28.34	28.64	28.57	7592.62	2144.00	1782.04
10^{-3}	283.36	286.28	285.63	7822.71	2391.70	2030.97
10^{-2}	2825.20	2853.34	2847.09	10118.91	4861.54	4512.95
10^{-1}	27452.41	27641.10	27600.28	32620.12	28872.60	28628.26
1	219444.44	219444.44	219444.44	219444.44	219444.44	219444.44

Table B6

Analytical Hashin–Shtrikman and the three-point Beran-Molyneux bounds for the bulk modulus for phase contrast values for $\phi_1 \simeq 0.50$ phase volume fraction. The two columns identified by I and II given for the three-point bounds are created with the tabulated η_i and ζ_i values (see Eq. A.2) corresponding to the Gaussian random fields studied in the Refs. Roberts and Teubner (1995) and Roberts and Garboczi (2002), respectively. $E_1 = 79$ GPa and $\nu_1 = 0.44$ which gives $K_1 \simeq 219444.44$ MPa and $G_1 \simeq 27430.56$ MPa.

$\frac{E_2}{E_1}$ [−]	lower bounds			upper bounds		
	$K_{L,HS}$ [MPa]	$K_{L,BM,I}$ [MPa]	$K_{L,BM,II}$ [MPa]	$K_{U,HS}$ [MPa]	$K_{U,BM,I}$ [MPa]	$K_{U,BM,II}$ [MPa]
0	0.00	0.00	0.00	27430.56	15622.18	15673.26
10^{-4}	47.54	51.17	51.19	27464.16	15661.38	15712.44
10^{-3}	474.87	510.90	511.18	27766.33	16013.93	16064.76
10^{-2}	4695.68	5034.14	5036.69	30765.78	19506.14	19554.73
10^{-1}	42275.33	44105.35	44117.75	58688.63	51409.61	51440.39
1	219444.44	219444.44	219444.44	219444.44	219444.44	219444.44

Table B7

Analytical Hashin–Shtrikman and the three-point Milton-Phan-Tien bounds for the shear modulus for phase contrast values for $\phi_1 \simeq 0.20$ phase volume fraction. The two columns identified by I and II given for the three-point bounds are created with the tabulated η_i and ζ_i values (see Eq. A.2) corresponding to the Gaussian random fields studied in the Refs. Roberts and Teubner (1995) and Roberts and Garboczi (2002), respectively. $E_1 = 79$ GPa and $\nu_1 = 0.44$ which gives $K_1 \simeq 219444.44$ MPa and $G_1 \simeq 27430.56$ MPa.

$\frac{E_2}{E_1}$ [−]	lower bounds			upper bounds		
	$G_{\text{L,HS}}$ [MPa]	$G_{\text{L,MPT,I}}$ [MPa]	$G_{\text{L,MPT,II}}$ [MPa]	$G_{\text{U,HS}}$ [MPa]	$G_{\text{U,MPT,I}}$ [MPa]	$G_{\text{U,MPT,II}}$ [MPa]
0	0.00	0.00	0.00	3428.82	1460.51	1508.48
10^{-4}	4.34	4.60	4.61	3431.44	1463.97	1511.92
10^{-3}	43.39	45.93	46.08	3455.07	1495.10	1542.83
10^{-2}	429.74	453.49	454.94	3691.09	1804.70	1850.33
10^{-1}	3951.53	4075.15	4082.30	6029.63	4754.32	4783.06
1	27430.56	27430.56	27430.56	27430.56	27430.56	27430.56

Table B8

Analytical Hashin–Shtrikman and the three-point Milton-Phan-Tien bounds for the shear modulus for phase contrast values for $\phi_1 \simeq 0.50$ phase volume fraction. The two columns identified by I and II given for the three-point bounds are created with the tabulated η_i and ζ_i values (see Eq. A.2) corresponding to the Gaussian random fields studied in the Refs. Roberts and Teubner (1995) and Roberts and Garboczi (2002), respectively. $E_1 = 79$ GPa and $\nu_1 = 0.44$ which gives $K_1 \simeq 219444.44$ MPa and $G_1 \simeq 27430.56$ MPa.

$\frac{E_2}{E_1}$ [−]	lower bounds			upper bounds		
	$G_{\text{L,HS}}$ [MPa]	$G_{\text{L,MPT,I}}$ [MPa]	$G_{\text{L,MPT,II}}$ [MPa]	$G_{\text{U,HS}}$ [MPa]	$G_{\text{U,MPT,I}}$ [MPa]	$G_{\text{U,MPT,II}}$ [MPa]
0	0.00	0.00	0.00	9974.75	7827.60	7836.18
10^{-4}	9.14	12.77	12.79	9976.97	7830.74	7839.31
10^{-3}	91.14	127.00	127.18	9996.96	7858.97	7867.51
10^{-2}	885.54	1202.68	1204.24	10196.31	8139.23	8147.40
10^{-1}	6957.99	8072.01	8076.48	12137.41	10752.63	10757.80
1	27430.56	27430.56	27430.56	27430.56	27430.56	27430.56

Table B9

Computed effective gold-epoxy composite properties for various volume fractions and boundary conditions. $E_1 = 79$ GPa and $\nu_1 = 0.44$ which gives $K_1 \simeq 219444.44$ MPa and $G_1 \simeq 27430.56$ MPa.

ϕ_{gold} [−]	Periodic BC				Kinematically Uniform BC			
	$K^\star$ [MPa]	$G^\star$ [MPa]	$\nu^\star$ [−]	$A_U^\star$ [−]	$K^\star$ [MPa]	$G^\star$ [MPa]	$\nu^\star$ [−]	$A_U^\star$ [−]
0.20	2161.21 ± 39.26	959.34 ± 23.51	0.3065 ± 0.0012	8.38×10^{-3}	2513.93 ± 48.75	1198.91 ± 29.83	0.2943 ± 0.0011	4.70×10^{-3}
0.25	2846.48 ± 62.44	1345.37 ± 36.02	0.2959 ± 0.0010	1.32×10^{-2}	3373.38 ± 70.12	1682.38 ± 40.77	0.2862 ± 0.0009	7.41×10^{-3}
0.30	3903.67 ± 106.24	1920.76 ± 55.74	0.2887 ± 0.0007	1.72×10^{-2}	4639.14 ± 112.33	2357.40 ± 57.51	0.2827 ± 0.0007	1.06×10^{-2}
0.35	5454.15 ± 127.60	2722.55 ± 63.21	0.2860 ± 0.0004	1.82×10^{-2}	6415.70 ± 132.64	3245.84 ± 62.78	0.2835 ± 0.0005	1.21×10^{-2}
0.40	7588.80 ± 145.66	3760.47 ± 65.27	0.2874 ± 0.0004	1.66×10^{-2}	8784.20 ± 155.91	4348.38 ± 63.96	0.2875 ± 0.0004	1.18×10^{-2}
0.45	10370.51 ± 116.74	5014.16 ± 47.53	0.2918 ± 0.0004	1.40×10^{-2}	11795.00 ± 125.61	5639.16 ± 44.85	0.2938 ± 0.0005	1.06×10^{-2}
0.50	13934.85 ± 83.85	6467.20 ± 28.88	0.2990 ± 0.0003	1.10×10^{-2}	15574.02 ± 84.15	7100.60 ± 25.65	0.3021 ± 0.0003	8.77×10^{-3}

Appendix C. A summary of the influence of the selected boundary conditions on the macroscopic material response

Based on the determined RVE size, computed apparent (KUBC) and effective (PBC) elastic properties tabulated in Tables B.3 and B.4 show that kinematically uniform boundary conditions overestimate the effective properties for the range of observed property contrast. The difference in

Table C1

Ratio of computed apparent (KUBC) and effective (PBC) elastic properties for various phase contrast values for $\phi_1 \simeq 0.20$ and $\phi_1 \simeq 0.50$ phase volume fraction at RVE size determined using periodic boundary conditions. $E_1 = 79$ GPa and $\nu_1 = 0.44$ which gives $K_1 \simeq 219444.44$ MPa and $G_1 \simeq 27430.56$ MPa.

$\frac{E_2}{E_1}$ [−]	$\phi_1 \simeq 0.20$		$\phi_1 \simeq 0.50$	
	$\frac{K_{\text{KUBC}}^\star}{K_{\text{PBC}}^\star}$ [−]	$\frac{G_{\text{KUBC}}^\star}{G_{\text{PBC}}^\star}$ [−]	$\frac{K_{\text{KUBC}}^\star}{K_{\text{PBC}}^\star}$ [−]	$\frac{G_{\text{KUBC}}^\star}{G_{\text{PBC}}^\star}$ [−]
0	12.34	10.47	1.17	1.13
10^{-4}	5.05	5.70	1.17	1.13
10^{-3}	1.81	2.55	1.16	1.13
10^{-2}	1.10	1.32	1.10	1.10
10^{-1}	1.01	1.04	1.02	1.04
1	1	1	1	1

between estimations reduces with decreasing phase contrast and finally vanishes for the case where both phases feature identical properties, see Table C.10. We judge from the demonstrated results for $\phi_1 \simeq 0.20$ and $\phi_1 \simeq 0.50$ that, at this volume element size the boundary condition influence can be disregarded only for the material contrast of $E_2/E_1 > 10^{-1}$.

References

Al-Ketan, O., Al-Rub, R.K.A., Rowshan, R., 2017. Mechanical properties of a new type of architected interpenetrating phase composite materials. Adv. Mater. Technol. 2 (2), 1600235. https://doi.org/10.1002/admt.201600235. ISSN 2365-709X, 1600235

Bargmann, S., Klusemann, B., Markmann, J., Schnabel, J.E., Schneider, K., Soyarslan, C., Wilmers, J., 2018. Generation of 3D representative volume elements for heterogeneous materials: a review. Progress Mater. Sci. 96, 322–384. https://doi.org/10.1016/j.pmatsci.2018.02.003.

Bargmann, S., Soyarslan, C., Husser, E., Konchakova, N., 2016. Materials based design of structures: computational modeling of the mechanical behavior of gold-polymer nanocomposites. Mech. Mater. 94, 53–65. https://doi.org/10.1016/j.mechmat.2015.11.008. ISSN 0167–6636, http://www.sciencedirect.com/science/article/pii/S0167663615002422

Bates, F.S., Schulz, M.F., Khandpur, A.K., Förster, S., Rosedale, J.H., Almdal, K., Mortensen, K., 1994. Fluctuations, conformational asymmetry and block copolymer phase behaviour. Faraday Discuss. 98, 7–18.

Beran, M.J., Molyneux, J., 1966. Use of classical variational principles to determine bounds for the effective bulk modulus in heterogeneous media. Quart. Appl. Math. 24, 107–118.

Berk, N.F., 1991. Scattering properties of the leveled-wave model of random morphologies. Phys. Rev. A 44, 5069–5079. https://doi.org/10.1103/PhysRevA.44.5069.

Biener, J., Hodge, A.M., Hamza, A.V., Hsiung, L.M., Satcher Jr., J.H., 2005. Nanoporous au: a high yield strength material. J. Appl. Phys. 97 (2), 024301. https://doi.org/10.1063/1.1832742.

Biener, J., Hodge, A.M., Hayes, J.R., Volkert, C.A., Zepeda-Ruiz, L.A., Hamza, A.V., Abraham, F.F., 2006. Size effects on the mechanical behavior of nanoporous au. Nano Lett. 6 (10), 2379–2382. https://doi.org/10.1021/nl061978i. PMID: 17034115

Cahn, J.W., 1965. Phase separation by spinodal decomposition in isotropic systems. J. Chem. Phys. 42 (1), 93–99. https://doi.org/10.1063/1.1695731.

Cahn, J.W., Hilliard, J.E., 1959. Free energy of a nonuniform system. III. nucleation in a two-component incompressible fluid. J. Chem. Phys. 31 (3), 688–699. https://doi.org/10.1063/1.1730447.

Carolan, D., Chong, H., Ivankovic, A., Kinloch, A., Taylor, A., 2015. Co-continuous polymer systems: a numerical investigation. Comput. Mater. Sci. 98, 24–33. https://doi.org/10.1016/j.commatsci.2014.10.039. ISSN 0927-0256

Chen, Y.C.K., Chu, Y.S., Yi, J., McNulty, I., Shen, Q., Voorhees, P.W., Dunand, D.C., 2010. Morphological and topological analysis of coarsened nanoporous gold by x-ray nanotomography. Appl. Phys. Lett. 96 (4), 043122. https://doi.org/10.1063/1.3285175.

Eidel, B., Fischer, A., 2018. The heterogeneous multiscale finite element method for the homogenization of linear elastic solids and a comparison with the FE2 method. Comput. Methods Appl. Mech. Eng. 329, 332–368. https://doi.org/10.1016/j.cma.2017.10.001. ISSN 0045–7825

Elsner, B.A.M., Müller, S., Bargmann, S., Weissmüller, J., 2017. Surface excess elasticity of gold: AB initio coefficients and impact on the effective elastic response of nanowires. Acta Mater. 124, 468–477. ISSN 1359–6454

Erlebacher, J., Aziz, M.J., Karma, A., Dimitrov, N., Sieradzki, K., 2001. Evolution of nanoporosity in dealloying. Nature 410 (6827), 450–453.

Fish, J., 2014. Practical Multiscaling. John Wiley and Sons, Chichester.

Fish, J., Fan, R., 2008. Mathematical homogenization of nonperiodic heterogeneous media subjected to large deformation transient loading. Int. J. Numer. Methods Eng. 76 (7), 1044–1064.

Fish, J., Shek, K., Pandheeradi, M., Shephard, M.S., 1997. Computational plasticity for composite structures based on mathematical homogenization: theory and practice. Comput. Methods Appl. Mech. Eng. 148 (1), 53–73. https://doi.org/10.1016/S0045-7825(97)00030-3. ISSN 0045–7825, http://www.sciencedirect.com/science/article/pii/S0045782597000303

Gibson, L.J., Ashby, M.F., 1997. Cellular solids: structure and properties. Cambridge Solid State Science Series, 2 ed. Cambridge University Press.

Griffiths, E., Bargmann, S., Reddy, B., 2017. Elastic behaviour at the nanoscale of innovative composites of nanoporous gold and polymer. Extreme Mech. Lett. 17, 16–23. ISSN 2352–4316

Hashin, Z., Shtrikman, S., 1963. A variational approach to the theory of the elastic behaviour of multiphase materials. J. Mech. Phys. Solids 11 (2), 127–140. https://doi.org/10.1016/0022-5096(63)90060-7. ISSN 0022–5096, http://www.sciencedirect.com/science/article/pii/0022509663900607

Hill, R., 1952. The elastic behaviour of a crystalline aggregate. Proc. Phys. Soc. Sect. A 65 (5), 349.

Hill, R., 1972. On constitutive macro-variables for heterogeneous solids at finite strain. Proc. R. Soc. Lond. A Math. Phys. Eng. Sci. 326 (1565), 131–147. https://doi.org/10.1098/rspa.1972.0001. ISSN 0080–4630

Hodge, A., Biener, J., Hayes, J., Bythrow, P., Volkert, C., Hamza, A., 2007. Scaling equation for yield strength of nanoporous open-cell foams. Acta Mater. 55 (4), 1343–1349. https://doi.org/10.1016/j.actamat.2006.09.038. ISSN 1359–6454

Hu, K., 2017. Micromechanical and Three-Dimensional Microstructural Characterization of Nanoporous Gold-Epoxy Composites. Hamburg University of Technology Ph.d. thesis.

Hu, K., Ziehmer, M., Wang, K., Lilleodden, E.T., 2016. Nanoporous gold: 3D structural analyses of representative volumes and their implications on scaling relations of mechanical behaviour. Philosoph. Mag. 96, 1–14.

Huber, N., Viswanath, R.N., Mameka, N., Markmann, J., Weissmüller, J., 2014. Scaling laws of nanoporous metals under uniaxial compression. Acta. Materialia. 67, 252–265.

Jiao, J., Huber, N., 2017. Deformation mechanisms in nanoporous metals: effect of ligament shape and disorder. Comput. Mater. Sci. 127, 194–203. https://doi.org/10.1016/j.commatsci.2016.10.035. ISSN 0927-0256, http://www.sciencedirect.com/science/article/pii/S0927025616305481

Lai, M., Kulak, A.N., Law, D., Zhang, Z., Meldrum, F.C., Riley, D.J., 2007. Profiting from nature: macroporous copper with superior mechanical properties. Chem. Commun. 3547–3549.

Leitner, A., Maier-Kiener, V., Kiener, D., 2018. High temperature flow behavior of ultrastrong nanoporous au assessed by spherical nanoindentation. Nanomaterials 8 (6), 366. https://doi.org/10.3390/nano8060366. ISSN 2079–4991

Lührs, L., Soyarslan, C., Markmann, J., Bargmann, S., Weissmüller, J., 2016. Elastic and plastic poisson's ratios of nanoporous gold. Scripta Mater. 110, 65–69. https://doi.org/10.1016/j.scriptamat.2015.08.002. ISSN 1359–6462

Lukkassen, D., Persson, L.E., Wall, P., 1995. Some engineering and mathematical aspects on the homogenization method. Compos. Eng. 5 (5), 519–531. https://doi.org/10.1016/0961-9526(95)00025-I. ISSN 0961–9526

Mameka, N., Wang, K., Markmann, J., Lilleodden, E.T., Weissmüller, J., 2016. Nanoporous gold-testing macro-scale samples to probe small-scale mechanical behavior. Mater. Res. Lett. 4 (1), 27–36. https://doi.org/10.1080/21663831.2015.1094679.

Markenscoff, X., Dascalu, C., 2012. Asymptotic homogenization analysis for damage amplification due to singular interaction of micro-cracks. J. Mech. Phys. Solids 60 (8), 1478–1485. https://doi.org/10.1016/j.jmps.2012.05.096

McBride, A., Mergheim, J., Javili, A., Steinmann, P., Bargmann, S., 2012. Micro-to-macro transitions for heterogeneous material layers accounting for in-plane stretch. J. Mech. Phys. Solids 60 (6), 1221–1239. https://doi.org/10.1016/j.jmps.2012.01.003. ISSN 0022–5096

McCue, I., Benn, E., Gaskey, B., Erlebacher, J., 2016. Dealloying and dealloyed materials. Ann. Rev. Mater. Res. 46 (1), 263–286. https://doi.org/10.1146/annurev-matsci-070115-031739.

Michielsen, K., Stavenga, D., 2008. Gyroid cuticular structures in butterfly wing scales: biological photonic crystals. J. R. Soc. Int. 5 (18), 85–94. https://doi.org/10.1098/rsif.2007.1065.

Miehe, C., Koch, A., 2002. Computational micro-to-macro transitions of discretized microstructures undergoing small strains. Arch. Appl. Mech. 72 (4), 300–317. https://doi.org/10.1007/s00419-002-0212-2.

Milton, G.W., 1981. Bounds on the electromagnetic, elastic, and other properties of two-component composites. Phys. Rev. Lett. 46, 542–545. https://doi.org/10.1103/PhysRevLett.46.542.

Milton, G.W., Phan-Thien, N., 1982. New bounds on effective elastic Moduli of two-component materials. Proc. R. Soc. Lond. Ser. A, Math. Phys. Sci. 380 (1779), 305–331. ISSN 00804630, http://www.jstor.org/stable/2397305

Ostoja-Starzewski, M., 2007. Microstructural Randomness and Scaling in Mechanics of Materials, 1 ed. CRC Press.

Ostoja-Starzewski, M., Kale, S., Karimi, P., Malyarenko, A., Raghavan, B., Ranganathan, S., Zhang, J., 2016. Chapter two - scaling to RVE in random media. Advances in Applied Mechanics. 49. Elsevier, pp. 111–211. Doi: https://doi.org/10.1016/bs.aams.2016.07.001

Pahr, D.H., Zysset, P.K., 2008. Influence of boundary conditions on computed apparent elastic properties of cancellous bone. Biomech. Model. Mechanobiol. 7 (6), 463–476. https://doi.org/10.1007/s10237-007-0109-7. ISSN 1617–7940

Quintanilla, J., 1999. Microstructure and properties of random heterogeneous materials: a review of theoretical results. Polymer Eng. Sci. 39 (3), 559–585. https://doi.org/10.1002/pen.11446. ISSN 1548–2634

Ranganathan, S.I., Ostoja-Starzewski, M., 2008. Universal elastic anisotropy index. Phys. Rev. Lett. 101, 055504. https://doi.org/10.1103/PhysRevLett.101.055504.

Roberts, A.P., Garboczi, E.J., 2002. Computation of the linear elastic properties of random porous materials with a wide variety of microstructure. Proc. R. Soc. Lond. A Math. Phys. Eng. Sci. 458 (2021), 1033–1054. https://doi.org/10.1098/rspa.2001.0900. ISSN 1364–5021

Roberts, A.P., Knackstedt, M.A., 1996. Structure-property correlations in model composite materials. Phys. Rev. E 54, 2313–2328. https://doi.org/10.1103/PhysRevE.54.2313.

Roberts, A.P., Teubner, M., 1995. Transport properties of heterogeneous materials derived from gaussian random fields: bounds and simulation. Phys. Rev. E 51, 4141–4154. https://doi.org/10.1103/PhysRevE.51.4141.

Rösner, H., Parida, S., Kramer, D., Volkert, C.A., Weissmüller, J., 2007. Reconstructing a nanoporous metal in three dimensions: an electron tomography study of dealloyed gold leaf. Adv. Eng. Mater. 9 (7), 535–541. https://doi.org/10.1002/adem.200700063. ISSN 1527–2648

Saane, S., Mangipudi, K., Loos, K., Hosson, J.D., Onck, P., 2014. Multiscale modeling of charge-induced deformation of nanoporous gold structures. J. Mech. Phys. Solids 66, 1–15. https://doi.org/10.1016/j.jmps.2014.01.007. ISSN 0022–5096

Sab, K., Nedjar, B., 2005. Periodization of random media and representative volume element size for linear composites. Comptes Rendus Mécanique 333 (2), 187–195. https://doi.org/10.1016/j.crme.2004.10.003. ISSN 1631-0721

Soyarslan, C., Argeso, H., Bargmann, S., 2018a. Skeletonization-based beam finite element models for stochastic bicontinuous materials: Application to simulations of nanoporous gold. J. Mater. Res. 33 (20), 3371–3382. https://doi.org/10.1557/jmr.2018.244.

Soyarslan, C., Bargmann, S., Pradas, M., Weissmüller, J., 2018b. 3D Stochastic bicontinuous microstructures: generation, topology and elasticity. Acta Mater. 149, 326–340. https://doi.org/10.1016/j.actamat.2018.01.005. ISSN 1359–6454

Soyarslan, C., Husser, E., Bargmann, S., 2017. Effect of surface elasticity on the elastic response of nanoporous gold. J. Nanomech. Micromech. 7 (4). https://doi.org/10.1061/(ASCE)NM.2153-5477.0000126.

Sun, X.Y., Xu, G.K., Li, X., Feng, X.Q., Gao, H., 2013. Mechanical properties and scaling laws of nanoporous gold. J. Appl. Phys. 113 (2), 023505. https://doi.org/10.1063/1.4774246.

Suquet, P.M., 1987. Elements of Homogenization Theory for Inelastic Solid Mechanics. Springer-Verlag, Berlin, Heidelberg, New York. 194–275

Terada, K., Hori, M., Kyoya, T., Kikuchi, N., 2000. Simulation of the multi-scale convergence in computational homogenization approaches. Int. J. Solids Struct. 37 (16), 2285–2311. https://doi.org/10.1016/S0020-7683(98)00341-2. ISSN 0020–7683

Teubner, M., 1991. Level surfaces of gaussian random fields and microemulsions. EPL (Europhys. Lett.) 14 (5), 403.

Torquato, S., 1991. Random heterogeneous media: microstructure and improved bounds on effective properties. ASME. Appl. Mech. Rev. 44 (2), 37–76.

Torquato, S., 2002. Random Heterogeneous Materials: Microstructure and Macroscopic Properties. Springer New York, New York, NY. ISBN 978-1-4757-6355-3

Volkert, C.A., Lilleodden, E.T., Kramer, D., Weissmüller, J., 2006. Approaching the theoretical strength in nanoporous au. Appl. Phys. Lett. 89 (6), 061920.

Walpole, L., 1969. On the overall elastic Moduli of composite materials. J. Mech. Phys. Solids 17 (4), 235–251. https://doi.org/10.1016/0022-5096(69)90014-3. ISSN 0022–5096, http://www.sciencedirect.com/science/article/pii/0022509669900143

Wang, K., 2015. Composites of Nanoporous Gold and Polymer. Hamburg University of Technology Ph.d. thesis.

Wang, K., Weissmüller, J., 2013. Composites of nanoporous gold and polymer. Adv. Mater. 25 (9), 1280–1284. https://doi.org/10.1002/adma.201203740. ISSN 1521–4095

Wang, L., Lau, J., Thomas, E.L., Boyce, M.C., 2011. Co-continuous composite materials for stiffness, strength, and energy dissipation. Adv. Mater. 23 (13), 1524–1529. https://doi.org/10.1002/adma.201003956. ISSN 1521–4095

Weissmüller, J., Newman, R.C., Jin, H.J., Hodge, A.M., Kysar, J.W., 2009. Nanoporous Metals by Alloy Corrosion: Formation and Mechanical Properties, vol. 34. Materials Research Society, Warrendale, PA, ETATS-UNIS.

Weissmüller, J., Viswanath, R.N., Kramer, D., Zimmer, P., Würschum, R., Gleiter, H., 2003. Charge-induced reversible strain in a metal. Science 300 (5617), 312–315.

Xia, R., Wu, R.N., Liu, Y.L., Sun, X.Y., 2015. The role of computer simulation in nanoporous metals - a review. Materials 8 (8), 5060–5083. https://doi.org/10.3390/ma8085060. ISSN 1996-1944

Yang, W., Zheng, X.G., Wang, S.G., Jin, H.J., 2018. Nanoporous aluminum by galvanic replacement: dealloying and inward-growth plating. J. Electrochem. Soc. 165 (9), C492–C496. https://doi.org/10.1149/2.0881809jes. http://jes.ecsdl.org/content/165/9/C492.abstract

Yang, Y., Ma, F., Lei, C., Liu, Y., Li, J., 2013. Nonlinear asymptotic homogenization and the effective behavior of layered thermoelectric composites. J. Mech. Phys. Solids 61 (8), 1768–1783.

Zinchenko, O., Raedt, H.D., Detsi, E., Onck, P., Hosson, J.D., 2013. Nanoporous gold formation by dealloying: a metropolis monte carlo study. Comput. Phys. Commun. 184 (6), 1562–1569. https://doi.org/10.1016/j.cpc.2013.02.004. ISSN 0010–4655